Comparison of satellite reflectance algorithms for estimating chlorophyll-*a* in a temperate reservoir using coincident hyperspectral aircraft imagery and dense coincident surface observations

Richard Beck [a,*], Shengan Zhan [a], Hongxing Liu [a], Susanna Tong [a], Bo Yang [a], Min Xu [a], Zhaoxia Ye [a], Yan Huang [a], Song Shu [a], Qiusheng Wu [a], Shujie Wang [a], Kevin Berling [a], Andrew Murray [a], Erich Emery [b], Molly Reif [c], Joseph Harwood [c], Jade Young [d], Christopher Nietch [e], Dana Macke [e], Mark Martin [f], Garrett Stillings [f], Richard Stump [f], Haibin Su [h]

[a] Department of Geography, University of Cincinnati, Cincinnati, OH 45221, USA
[b] U.S. Army Corps of Engineers, Great Lakes and Ohio River Division, Cincinnati, OH 45202, USA
[c] U.S. Army Corps of Engineers, ERDC, JALBTCX, Kiln, MS 39556, USA
[d] U.S. Army Corps of Engineers, Louisville District, Water Quality, Louisville, KY 40202, USA
[e] U.S. Environmental Protection Agency, Cincinnati, OH 45268, USA
[f] Kentucky Department of Environmental Protection, Division of Water, Frankfort, KY 40601, USA
[g] National Oceanic and Atmospheric Administration, National Ocean Service, Silver Spring, MD, USA
[h] Department of Physics and Geosciences, Texas A&M Kingsville, Kingsville, TX 78363-8202, USA

ARTICLE INFO

ABSTRACT

We compared 10 established and 2 new satellite reflectance algorithms for estimating chlorophyll-*a* (Chl-*a*) in a temperate reservoir in southwest Ohio using coincident hyperspectral aircraft imagery and dense coincident surface observations collected within 1 h of image acquisition to develop simple proxies for algal blooms in water bodies sensitive to algal blooms (especially toxic or harmful algal blooms (HABs)) and to facilitate portability between multispectral satellite imagers for regional algal bloom monitoring. All algorithms were compared with narrow band hyperspectral aircraft images. These images were subsequently upscaled spectrally and spatially to simulate 5 current and near future satellite imaging systems. Established and new Chl-*a* algorithms were then applied to the synthetic satellite images and compared to coincident surface observations of Chl-*a* collected from 44 sites within 1 h of aircraft acquisition of the imagery. We found several promising algorithm/satellite imager combinations for routine Chl-*a* estimation in smaller inland water bodies with operational and near-future satellite systems. The CI, MCI, FLH, NDCI, 2BDA and 3 BDA Chl-*a* algorithms worked well with CASI imagery. The NDCI, 2BDA, and 3BDA Chl-*a* algorithms worked well with simulated WorldView-2 and 3, Sentinel-2, and MERIS-like imagery. NDCI was the most widely applicable Chl-*a* algorithm with good performance for CASI, WorldView 2 and 3, Sentinel-2 and MERIS-like imagery and limited performance with MODIS imagery. A new fluorescence line height "greenness" algorithm yielded the best Chl-*a* estimates with simulated Landsat-8 imagery.

© 2016 Elsevier Inc. All rights reserved.

1. Introduction

Blooms of cyanobacteria may release toxins in response to yet to be determined environmental triggers, although high nutrient and light levels appear important controls on toxin production (Ohio EPA, 2012). According to the U.S. Army Corps of Engineers (USACE) and U.S. Geological Survey (USGS) there has been a noticeable increase in problems associated with harmful algal blooms (HABs). (Graham, 2006; Linkov, Satterstrom, Loney, & Steevans, 2009). HABs are now a global problem in 45 countries worldwide and have been implicated in animal deaths in at least 27 US states (Graham, 2006). HABs produce dermatoxins, hepatoxins and neurotoxins (USEPA, 2012). Contact can cause liver and kidney toxicity and neurotoxicity resulting in headaches,

* Corresponding author.
E-mail addresses: richard.beck@uc.edu (R. Beck), zhansn@mail.uc.edu (S. Zhan), hongxing.liu@uc.edu (H. Liu), susana.tong@uc.edu (S. Tong), yangb2@mail.uc.edu (B. Yang), xum4@mail.uc.edu (M. Xu), yeza@ucmail.uc.edu (Z. Ye), huang2y2@ucmail.uc.edu (Y. Huang), shusg@mail.uc.edu (S. Shu), wuqe@mail.uc.edu (Q. Wu), wang2sj@mail.uc.edu (S. Wang), berlinkj@mail.uc.edu (K. Berling), murraya2@mail.uc.edu (A. Murray), erich.b.emery@usace.army.mil (E. Emery), molly.k.reif@usace.army.mil (M. Reif), joseph.h.harwood@usace.army.mil (J. Harwood), jade.l.young@usace.army.mil (J. Young), nietch.christopher@epa.gov (C. Nietch), macke.dana@epa.gov (D. Macke), mark.martin@ky.gov (M. Martin), garrett.stillings@ky.gov (G. Stillings), richard.stumpf@noaa.gov (R. Stump), haibin.su@tamuk.edu (H. Su).

numbness, dizziness, difficulty breathing and in rare cases, death (Linkov et al., 2009). The World Health Organization guidelines for drinking water set a standard for microcystin LR, a prevalent cyanobacteria toxin, at or below 1 ppb. The Ohio Department of Health issues Public Health Advisories when microcystin levels exceed 6 ppb and No Contact Advisories are issued when microcystin levels exceed 20 ppb.

Up to 2006, Graham (2006) noted that most HAB research focused on marine ecosystems and indentified four critical research needs: 1) research on the occurrence of freshwater HABs, 2) reliable techniques for algal identification and enumeration, 3) long-term studies of individual lakes, reservoirs and rivers to identify the environmental factors driving HAB formation, and 4) the development of methods for early detection and predictive models to allow resource managers more time to respond more effectively to potentially harmful conditions. Remote sensing from satellites has the potential to address HAB research needs 1, 3 and 4 (Shen, Xu, & Guo, 2012) via routine and consistent observations if the spatial resolution of the sensors is substantially less than the size of the water bodies being monitored, the temporal resolution of the satellite or satellites is meaningful given frequent cloud cover in temperate regions during those parts of the year when HABs are common and the images are available in a timely fashion and affordable to decision makers and researchers (Blondeau-Patissier, Gower, Dekker, Phinn, & Brando, 2014; Klemas, 2012; Stumpf & Tomlinson, 2005).

Remote sensing of algal blooms in ocean settings has been reviewed recently by Klemas (2012) and Blondeau-Patissier et al. (2014). Ocean settings are amenable to wide-field sensors such as MODIS, VIIRS and especially the MERIS follow-on which have wide swath widths and high temporal resolutions as noted in these recent reviews. In contrast, satellite remote sensing of smaller inland water bodies less than a few km across requires higher spatial resolution imagery (less than approximately 300 m GSD) implying narrow swath widths and lower temporal resolutions for individual satellites. Given the imaging and downlink constraints of sub 300 m spatial resolution satellite imagers and frequent cloud cover in temperate climates, satellite detection and monitoring of smaller inland reservoirs (common sources of drinking water) require multiple satellites in order to image such water bodies on a weekly or even bi-weekly basis. Constellations of several similar satellites such as Sentinels 2A and 2B are ideal for this task. Given the importance of monitoring drinking water supplies for potential HABs and the cost of remote sensing satellites the identification of the most portable algorithm or algorithms across multiple satellites capable of imaging smaller inland water bodies would allow one to create "meta-constellations" of existing and near-future satellites to maximize the temporal resolution of satellite monitoring of these water bodies. This study compares the performance of satellite reflectance algorithms for estimating chlorophyll-*a* in a temperate reservoir using synthetic satellite imagery or multiple imaging satellites constructed from high spatial and spectral resolution hyperspectral aircraft imagery and dense coincident surface observations to extend the recent in-situ surface spectroradiometer study of inland tropical reservoirs by Augusto-Silva et al. (2014) to temperate inland reservoirs.

This study compares the performance of 12 algorithms for the estimation of Chl-*a* applied to coincident synthetic imagery for five satellite imagers using water quality measurements collected by the USACE, U.S. Environmental Protection Agency (USEPA), USGS, Kentucky Division of Water, and University of Cincinnati. Airborne hyperspectral imagery was upscaled to moderate resolution satellite data to develop specifications for a prototype multi-satellite monitoring system for HABs in our case study lake, Harsha Lake, in Southwest Ohio. We addressed the research needs expressed by the USACE, USEPA and USGS for HAB monitoring and analysis in freshwater lakes and rivers with a multi-resolution surface, airborne and satellite study using water quality measurements, high-resolution 1-meter airborne hyperspectral imagery upscaled to 1.8-, 20-, 30-, 250- and 300-meter multispectral satellite imagery.

Increasingly algal blooms, including some toxic or "harmful" algal blooms (a.k.a HABs), are affecting inland reservoirs, many of which are used as a source of drinking water (Graham, 2006). These HABs have made the development of satellite reflectance algorithms for the estimation of Chl-*a* and associated phytoplankton biomass a high research priority (Fig. 1). Although Chl-*a* algorithms do not differentiate between harmful and less harmful algal blooms, they are more easily adapted to existing satellite imaging systems than phycocyanin algorithms and may help water resource managers focus limited time and money on risk mitigation of *potential* HABs accordingly. A similar analysis of phycocyanin algorithms will be presented in a companion paper.

Chlorophyll-*a* (Chl-*a*) is a spectrally active compound in phytoplankton that is commonly used as a proxy for phytoplankton biomass (Morel & Prieur, 1977; Vos, Donze, & Bueteveld, 1986; Gitelson, Nikanorov, Sabo, & Szilagyi, 1986; Gitelson, Gritz, & Merzlyak, 2003; Wynne, Stumpf, Tomlinson, & Dyble, 2012; Stumpf, Wynne, Baker, & Fahnenstiel, 2012; Kudela et al., 2015) and is therefore a key indicator of water quality (Verdin, 1985; Ekstrand, 1992; Reif, 2011; Mishra & Mishra, 2012). Satellite reflectance algorithms for estimating Chl-*a* concentrations in tropical inland reservoirs were recently reviewed and evaluated by Augusto-Silva et al. (2014). Augusto-Silva et al. (2014) used surface point spectroradiometers to collect reflectance signatures of Chl-*a* laden reservoir waters in Brazil and then synthesized Medium Resolution Imaging Spectrometer (MERIS) as well as its similar follow-on Ocean and Land Color Instrument (OLCI) imagery before applying the established two-band-algorithm (2BDA), three-band-algorithm (3BDA) and Normalized Difference Chlorophyll Index (NDCI) reflectance algorithms for Chl-*a* estimation (Gitelson et al., 2003; Dall'Olmo & Gitelson, 2005; Mishra & Mishra, 2012). They found that the band spacings in these instruments were suitable for Chl-*a*

Fig. 1. Photographs of harmful (toxic) *Microcystis* algae blooms on the Ohio River (22 August 2008) and in Harsha (East Fork) Lake (30 May 2012). The Ohio River and contributing inland reservoirs such as Harsha Lake are primary sources of drinking water for more than 5 million people (photo credits: Ohio EPA and United States EPA).

estimation in combination with empirical calibration (Sauer, Roesler, Werdell, & Barnard, 2012).

The overarching goal of this study is to maximize temporal coverage of inland reservoirs for algal bloom detection by leveraging existing and near-future multispectral satellite imaging systems by identifying the most "portable" Chl-*a* algorithms (Augusto-Silva et al., 2014; Hu, Barnes, Qi, & Crcoran, 2015; Mishra & Mishra, 2012; Shen et al., 2012). The option of using multiple satellites to image algal blooms in inland waters is especially important in humid, temperate climates where intermittent cloud cover limits temporal resolution (Veryla, 1995). Therefore, this research follows the lead of Augusto-Silva et al. (2014) in that it is focused on comparing relatively simple, reflectance-signature-based algorithms that provide reasonable estimates of Chl-*a* concentrations and phytoplankton biomass with current and near-future multispectral satellite imagers. The ultimate goal of this research is to explore and expand remote sensing-based options that could be used for near-real-time monitoring of inland water quality (Dekker and Peters, 1993; Gitelson et al., 1993; Fraser, 1998; Glasgow, Burkholder, Reed, Lewitus, & Kleinman, 2004; Binding, Greenberg, & Bukata, 2013). These simple reflectance-signature-based proxies will be used to "red flag" potential problem areas for additional field-based investigations (Augusto-Silva et al., 2014).

The acquisition of satellite imagery to estimate phytoplankton biomass in inland reservoirs in the visible and near-infrared parts of the electromagnetic spectrum is subject to cloud cover. In addition, surface phytoplankton concentrations are influenced by wind (mixing and drifting) as well as changes in the nutrient flux and water temperature, among other variables. Phytoplankton communities, in general, are dynamic on the scale of days and sometimes hours (Hunter, Tyler, Willby, & Gilvear, 2008; Sawaya et al., 2003; Wang, Xia, Fu, & Sheng, 2004).

Moderate resolution satellites such as Landsat-8 can provide affordable sources of imagery for water quality monitoring in inland reservoirs (Mayo, Gitelson, Yacobi, & Ben-Avraham, 1995); however, their fixed revisit times, fixed observation angles and small constellations (usually a single satellite) limit their temporal resolution (e.g., 16 days for Landsat-8). It is therefore desirable to use a variety of low-cost sources of moderate spatial resolution satellite imagery from different satellites to increase temporal resolution and maximize the chances of successful image acquisition. Moderate resolution satellites such as Landsat-8, MERIS/OLCI, the Moderate Resolution Imaging Spectrometer (MODIS), and the upcoming Sentinel-2A & B constellation have a variety of both spatial resolutions and band configurations. Not all satellite algorithms can be applied to all existing moderate resolution satellite imagers accordingly.

This paper focuses on Chl-*a* because more of the existing satellite imagers are suited to sensing the near-infrared Chl-*a* reflectance peak than the narrow 620 nm peak associated phycocyanin which is indeed a potentially more direct indicator of *harmful* algal blooms. The larger number of satellite imagers capable of detecting the near-infrared Chl-*a* peak increases temporal resolution in cloudy mid-latitude climates. Therefore, we have focused our efforts on finding simple reflectance-signature-based Chl-*a* algorithms that are relatively "portable" between satellite imaging systems and have been evaluated with dense coincident surface observations. These moderate resolution satellite imaging systems may be used as a low-cost "first-cut" to identify potential problem areas that may be verified with coincident surface observations and high resolution imagers such as WorldView-2 and -3.

The identification of Chl-*a* algorithms that are portable across satellite imaging systems is also complicated by their differences in overpass times (variable atmosphere and surface conditions), differences in spatial and spectral resolutions and differences in radiometry. We have attempted to address the first problem, differing overpass times by generating coincident synthetic satellite imagery from hyperspectral imagery (Thonfeld, Feilhauer, & Menz, 2012), in a manner similar to that used by Augusto-Silva et al. (2014) with surface point spectroradiometers with simple linear spectral binning and spatial upscaling of aircraft hyperspectral imagery (Schlapfer, Boerner, & Schaepman, 1999; Jarecke, Barry, Pearlman, & Markham, 2001; Borge and Mortensen, 2002). Simulating simultaneous imagery from multiple satellites from hyperspectral imagery removes temporal variation of both the atmosphere and the water surface from the comparison of the Chl-*a* algorithms and requires only one set of coincident surface observations.

Statistically significant correlations between image derived indices and coincident surface observations suggest that the NOAA CI, FLH, NDCI, 2BDA and 3BDA Chl-*a* algorithms (Mishra & Mishra, 2012; Wynne et al., 2012) will be portable between hyperspectral and MERIS-like imagers and that the NDCI, 2BDA, and 3BDA Chl-*a* algorithms (Mishra & Mishra, 2012) will be portable between hyperspectral imagers, WorldView-2 and -3, and Sentinel-2, MERIS-like imagers and to a lesser degree MODIS-like imagers and are worthy of further testing with real post-launch imagery and time-series coincident surface observations in preparation for near-real-time algal bloom monitoring systems. A new fluorescence line height algorithm yields the best Chl-*a* estimates with simulated Landsat-8 imagery as described below.

2. Methods

2.1. Study area

The Ohio River and its tributaries, often including reservoirs, are the sources of drinking water for more than 5,000,000 people (Vicory, 2009) and the sites of recent algal blooms (including HABs). The quality of water in the Ohio River is routinely monitored by the Ohio River Valley Water Sanitation Commission (ORSANCO), USEPA, Ohio EPA, and USGS. The water levels in the Ohio and the East Fork of the Little Miami Rivers are monitored by the USACE and USGS. NOAA monitors meteorological variables at nearby Lunken Airport in eastern Cincinnati. Harsha Lake lies within the East Fork of the Little Miami River Watershed above its confluence with the Little Miami River which then flows into the Ohio River. The East Fork Watershed and Harsha Lake is the subject of a long-term, routine non-point water quality study conducted by the USACE, USEPA and Ohio EPA as part of the East Fork Little Miami River Watershed Cooperative (EFWCoop). In addition to being a source of drinking water, Harsha Lake has two public swimming beaches, hosts open water swimming and sculling events and is used extensively for recreational fishing. These economies are suffering from the algae problems. When combined with the water quality information resources, Harsha Lake becomes an excellent case study for several research issues related to HABs (Fig. 2).

2.2. Data sets

Our research used the following key data sets: airborne visible and near-infrared (VNIR) hyperspectral imagery of Harsha Lake and extensive, coincident surface spectral observations, laboratory measurements of water quality parameters and in situ water sensors. These data sets were used to develop and calibrate a set of numerical algorithms for mapping the quantitative estimation of Chl-*a* concentration.

We built upon the ongoing work of the multi-agency EFWCoop to accurately quantify algal communities and coincident water physiochemistries in Harsha Lake by establishing a partnership with the USACE Joint Airborne Lidar Bathymetry Technical Center of Expertise (JALBTCX) that supported an airborne survey using an Itres. Inc. Compact Airborne Spectrographic Imager (CASI)-1500 VNIR hyperspectral imager (HSI) mounted on a light aircraft. Research boats operated by the USACE, USEPA, Kentucky Division of Water and University of Cincinnati collected water quality and cyanobacteria data below the path of the aircraft within 1 h of image acquisition.
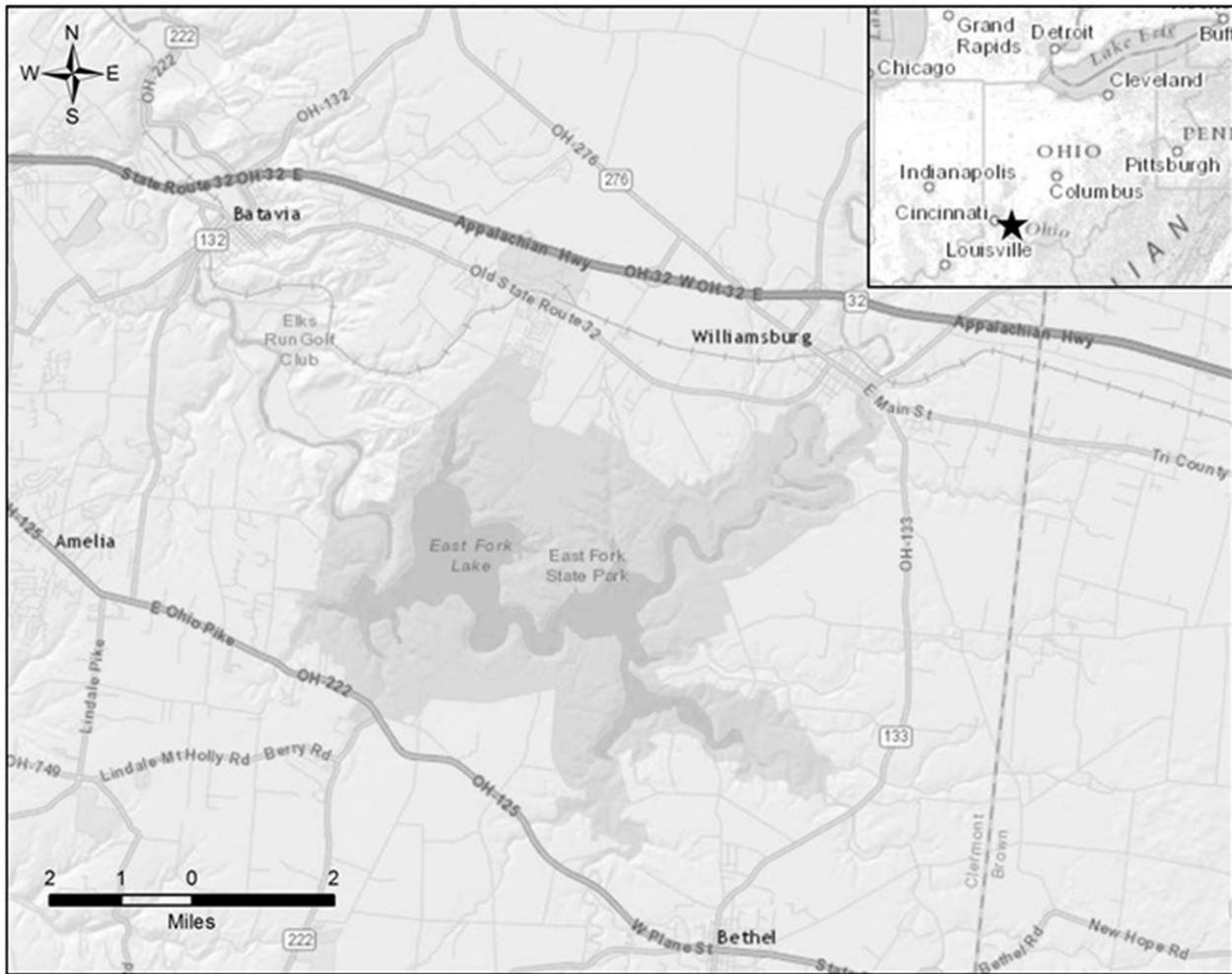
Fig. 2. Location map of Harsha (East Fork) Lake near Cincinnati, Ohio. The Ohio River and contributing inland water bodies such as Harsha Lake are primary sources of drinking water for more than 5 million people
(source: U.S. Army Corps of Engineers).

2.3. Field campaign

For this study, the JALBTCX was consulted to predict a date range in June with suitable survey conditions to acquire the hyperspectral images. The airborne survey was scheduled to meet a 20–60° solar elevation angle (30–70° solar zenith angle) flight window to reduce sun glint following USACE standard practice to allow for early morning image acquisitions, maximize flying time and the number of coincident field observations, and avoid cloud formation in humid summer weather conditions. This practice compares well with suggested solar elevation angles of 30–60° (Dekker and Peters, 1993) and 35–50° (Mustard et al., 2001) and allows us to avoid mid-day clouds with early morning flights. The JALBTCX determined that there would be two daily minimal sun glint windows for Harsha Lake from 15 through 29 June 2014 with good to excellent (reasonably low) Global Positioning System (GPS) Position Dilution of Precision (PDOP) values to enable precise aircraft ephemeris tracking during intervals of low cloud cover. Additional consultation with the National Weather Service (NWS) provided daily weather updates to identify days and times within the suitable survey window with cloud free or near cloud free conditions. This temporal filtering process resulted in the acquisition of aircraft-based hyperspectral imagery and coincident surface observations on the morning of 27 June 2014.

2.4. Airborne hyperspectral imagery acquisition and pre-processing

A CASI-1500 VNIR airborne hyperspectral imaging system was flown at an altitude of approximately 2000 m and acquired 48-band hyperspectral image strips 1466-meters wide at 1-meter spatial and 14 nanometer Full Width Half Maximum (FWHM) spectral resolution over a wavelength range of 371 to 1042 nm. JALBTCX personnel used in-house scripts and Itres' processing executables to convert the raw data, extract navigation data, accurately process the navigation, and produce radiance image strips. Radiance image strips were then geometrically corrected and mosaicked using precisely computed boresight values and a high resolution digital elevation model (DEM). Overlapping pixels were chosen based on the smallest off-nadir angle when mosaicking. Following this process, the mosaicked image was then used as input into Exelis ENVI Software's Fast Line of Sight Atmospheric Analysis of Hypercubes (FLAASH) module. The Mid-Latitude Summer (MLS) MODTRAN® model was chosen for correcting the column water vapor and water retrieval was set at 940 nm. The initial scene visibility was set at >40 km as the atmospheric conditions were clear with little to no haze while the collection occurred. The final output resulted in an atmospherically corrected, spectrally polished reflectance image. TAFKAA/ATREM algorithms may be more typically used to atmospherically correct open ocean image scenes; however, the mosaicked

reflectance image processed in this study primarily consisted of land (more than 80% of the total pixels were land), thus we chose a correction algorithm that offered flexibility to handle contributions from both land and water. Tests with extracted water pixel FLAASH reflectance spectra after atmospheric correction are similar to water field spectral measurements as shown in Fig. 5.

In order to accurately map and quantify algal blooms, we created high-resolution maps of Chl-*a* concentration based on airborne hyperspectral images with coincident surface observations. Hyperspectral imaging data consist of many sensitive, narrow bands spanning a wide spectral range which allows for simultaneous retrieval of chlorophyll concentration, suspended sediment, and CDOM in the coastal and lake waters (Koponen, Pulliainen, Kallio, & Hallikainen, 2002, Giardino, Brando, Dekker, Strombeck, & Candiani, 2007). This paper focuses on Chlorophyll-*a* concentrations in smaller inland water bodies because most satellite imagers do not have a narrow band near 620 nm. We will consider those satellite imagers that do have a narrow band near 620 nm in a companion paper focused on phycocyanin algorithm performance.

2.5. Coincident surface observation procedures

A review of the literature and discussions with NOAA confirmed that Chl-*a* is a reasonable proxy for algal blooms (Klemas, 2012). Detection of Chl-*a* with multispectral and hyperspectral imagery has also been well documented by the same researchers although they debate which algorithms and sensors are most appropriate for any given water body (Alawadi, 2010; Allee & Johnson, 1999; Brivio, Giardino, & Zilioli, 2001; Cannizzaro & Carder, 2006; Choubey, 1994; Dekker & Peters, 1993; Dall'Olmo, Gitelson, & Rundquist, 2003; Fraser, 1998; Frohn & Autrey, 2009; Gitelson, 1992; Gower, King, & Goncalves, 2008; Han, Rundquist, Liu, Fraser, & Schalles, 1994; Kneubuhler et al., 2007; Matthews, Duncan, & Davison, 2001; Quibell, 1992; Rundquist, Han, Schalles, & Peake, 1996; Schalles, Schiebe, Starks, & Troeger, 1997; Stumpf et al., 2012; Thiemann & Kaufmann, 2002: Vos et al., 1986; Wynne et al., 2012; Zhao, Xing, Liu, Yang, & Wang, 2010). Therefore, this sampling program focused on collecting a large and dense set of coincident surface observations to evaluate both real and synthetic coincident (from aircraft hyperspectral) Landsat-8, MODIS, MERIS/OLCI, WorldView-2/-3, and Sentinel-2 images and algorithms with regard to the estimation of Chl-*a* concentrations and turbidity anomalies in relatively small inland water bodies (less than a few kilometers across). This study focused on a comparison of the performance of Chl-*a* algorithms (Table 2), and so direct discrimination between algal blooms and harmful algal blooms with imagery was not part of this study. Phycocyanin algorithms are compared in a separate study.

In order to compare the performance of Chl-*a* algorithms with CASI and several synthetic multispectral data sets we deployed four research boats and acquired 44 coincident surface observations on a 400 meter grid point spacing with YSI water quality sondes cross-calibrated by the US EPA Experimental Stream Facility. Surface observation collection was coordinated with the imaging aircraft via an air-to-ground radio. Each boat collected the following GPS location and time (and depth) referenced coincident surface observations:

1. Water samples from each sample point for laboratory measurements by the USEPA
2. ASD spectra to evaluate atmospheric correction of CASI imagery.
3. In situ sensor measurements of Chl-*a* indicator, phycocyanin indicator, turbidity, specific conductance, pH, water temperature, and dissolved oxygen.
4. Secchi depth measurements at each sample point – meters below surface.
5. GPS location- and date/time-referenced photos of surface water conditions at each sample point. All data were referenced to the WGS84

map datum and converted to the Universal Transverse Mercator (UTM) Zone 16 North map projection (Fig. 3).

Water samples grabbed at each of the coincident surface observation sites were analyzed using standard methods for several parameters. We used the sum of the Phaeophytin corrected Chl-*a* and Phaeophytin a (abbreviated according to standard US EPA practice as SUM ReCHL (µg/L)) as the measure of Chl-*a* for our coincident surface observation standard determined from the equations provided after extraction and spectrophotometric detection according to standard method 10200H-2.b: Spectrophotometric determination of chlorophyll in the presence of phaeophytin a (APHA et al., 2012).

2.6. Synthetic satellite imagery

Hyperspectral bands were spectrally averaged with equal weight using "Band Math" in ENVI to produce synthetic satellite image bands for Landsat-8, Sentinel-2/MSI, Sentinel-3/MERIS/OLCI, MODIS, and WorldView-2/3, according to published specifications (DigitalGlobe, 2009, 2014; ESA, 2012, 2013; USGS, 2015; Lindsey & Herring, 2001). Given our focus on smaller inland water bodies we have not simulated image data sets with bands with spatial resolutions coarser than 300 m.

We used simple linear spectral binning of the CASI data to approximate all of the imagers because did not know the post-launch spectral response of Sentinel-2, WorldView-3 or of the MERIS/OLCI follow on imagers at the time of this study. Linear resampling of hyperspectral data introduces 1–3% RMS error or 6 to 8% relative error and other techniques may double or halve this error (Schlapfer et al., 1999). Broge and Mortensen (2002) studied greenness indices for terrestrial vegetation and recommended that spectral resampling should represent "the reflectance as an average value calculated over the full width of each new band" and that "Simple linear interpolation between spectral reflectances combined with band aggregation may be the most feasible way of spectral resampling." We have followed this method for the comparison of aquatic greenness indices presented here.

We chose to approximate all of the simulated imagers with the same simple band average calculations recommended by Broge and Mortensen (2002). We could have applied the Landsat-8, MODIS and predicted spectral MERIS/OLCI spectral response functions to the CASI data, and this would have required resampling 14 nm FWHM CASI imagery to approximately 1 nm FWHM using linear interpolation (Augusto-Silva et al., 2014) before re-binning to the spectral response functions of only some of the simulated imagers. Previous studies have concluded that even with careful modelling of spectral response functions, the radiometry of multispectral imagery simulated from hyperspectral imagery and real multispectral imagery may differ by up to twice pre-launch estimates (Jarecke et al., 2001) and associated spectral resampling may halve or double radiometric errors on the order of 6–8% associated with linear spectral resampling (Schlapfer et al., 1999). Therefore our choice of simple linear spectral resampling of the band configuration of the multispectral satellite imaging systems from narrow band airborne hyperspectral data and the resulting simulated radiometry are only approximations but are consistent between the synthetic imagers. The differing spatial resolutions between the different imagers are more problematic and introduce radiometric errors on the order of 10–32% in similar imaging spectrometers (Schlapfer, Schaepman, & Strobl, 2002) and result in complex trade-offs between band pass, sampling interval and signal-to-noise ratios that influence spectral detection capabilities (Swayze, Clark, Goetz, Chrien, & Gorelick, 2003).

Nonetheless, all of our results from the simple linear approximation method presented below are constructed from the same reflectance data set (the same atmospheric conditions) and are normalized to the same set of dense coincident surface observations. This method also eliminates the co-registration errors that complicate the radiometric comparison of real imagery acquired at different times (Thonfeld
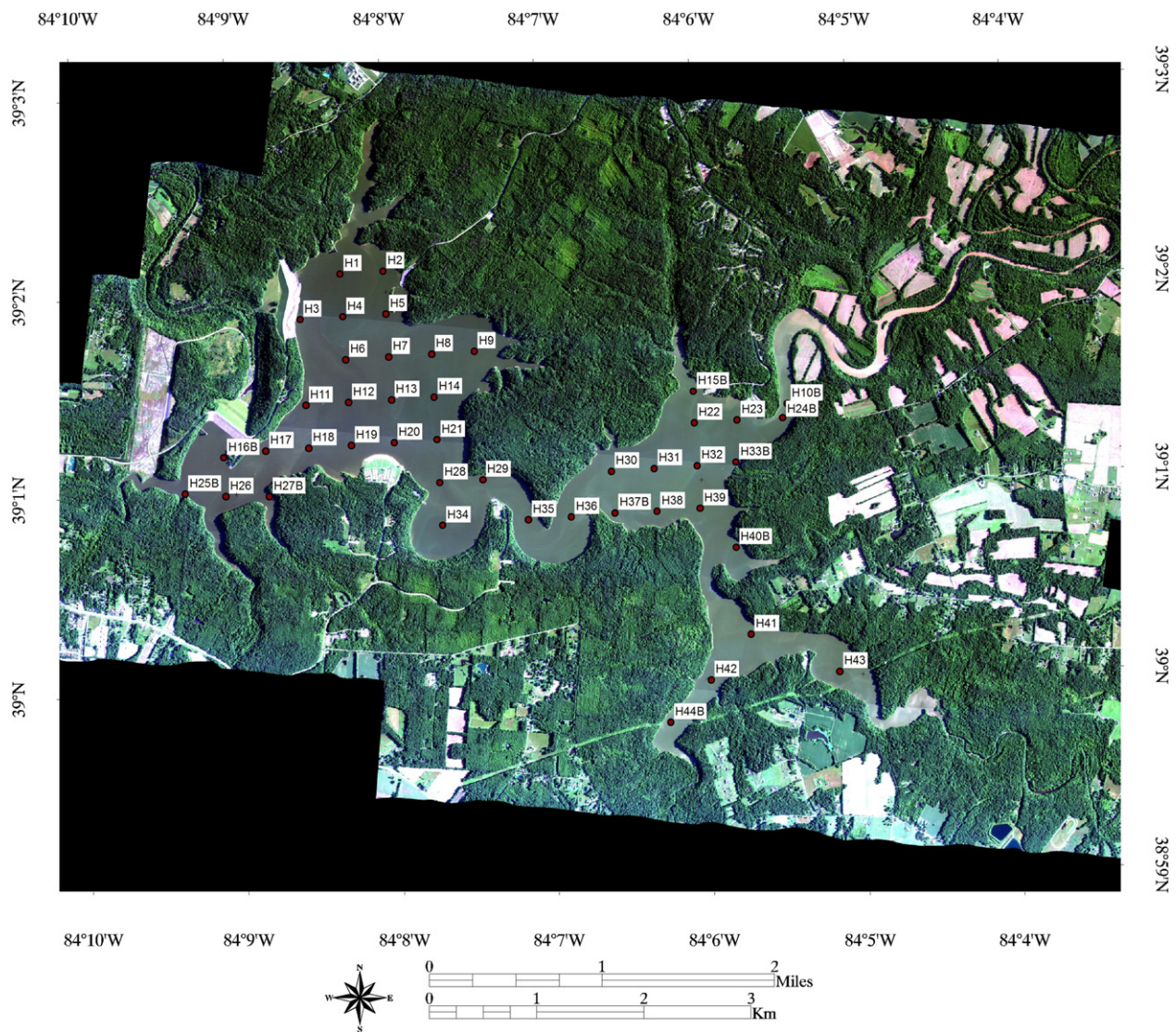
Fig. 3. Natural Color Image of Harsha (East Fork) Lake acquired with a CASI-1500 imager on 27 June 2014 with coincident surface observation locations used in this study. We acquired 44 coincident water quality sonde and water samples within 1 h of image acquisition to evaluate the performance of a variety of algorithms for estimating chlorophyll-*a* concentrations in a temperate reservoir for a variety of satellite imaging systems.

et al., 2012). These synthetic bands were then resampled to the appropriate spatial resolution using "Resize Data" in ENVI. The resulting synthetic band designations used in the subsequent analysis are shown in Table 1.

2.7. Image analysis

We extended the coincident synthetic sensor methodology of Augusto-Silva et al. (2014) to temperate inland reservoirs using aircraft acquired hyperspectral imagery (Mittenzwey, Ulrich, Gitelson, & Kondratiev, 1992; Kallio, 2000; Koponen et al., 2002) instead of surface based spectroradiometer data. Our aircraft imagery was also converted to reflectance and then artificially binned to create synthetic MERIS, MODIS, WorldView-2/-3, Sentinel-2 and Landsat-8 imagery that are "coincident" with a large coincident surface observation campaign as suggested by Reif (2011). We then applied the same algorithm set as Augusto-Silva et al. (2014) and extended it to include the Cyanobacterial Index (CI), Maximum Chlorophyll Index (MCI), Fluorescence Line Height (FLH), and Surface Algal Bloom Index (SABI) algorithms (Wynne et al., 2012; Binding et al., 2013; Zhao et al., 2010; Alawadi, 2010, respectively) as well as some new hybrid indices (this paper) to create a list of algorithm options by satellite imaging system

for water resource managers concerned with inland water quality (Chipman, Olmanson, & Gitelson, 2009). A table of Chl-*a* algorithms and their abbreviations as used in this study and listed by imaging system is included in Table 1.

We used the Band Math function in ENVI 5.1 to apply the Cyanobacterial Index (CI) (Wynne et al., 2012), Maximum Chlorophyll Index (MCI) (Binding et al., 2013), Florescence Line Height (FLH) (Zhao et al., 2010), Normalized Difference Chlorophyll Index (NDCI) (Mishra & Mishra, 2012), 2BDA (Dall'Olmo & Gitelson, 2005), 3BDA (Gitelson et al., 2003) and KIVU (Brivio et al., 2001) algorithms to the original CASI reflectance data to establish a performance base-line before creating synthetic imagery that corresponds to the band spacing of currently operational WorldView-2 and -3, Landsat-8, MODIS and near-future Sentinel-2 and Sentinel-3 (MERIS-like OLCI) satellite imaging systems (Table 2).

Not all algorithms could be applied to all synthetic images due to band position, band spacing and band width constraints (Lathrop & Lillesand, 1986; Cairns, Dickson, & Atkinson, 1997). We focused on relatively simple reflectance-signature-based ratio and shape metric algorithms (Zhao et al., 2010; Mishra & Mishra, 2012) for the sake of simplicity, brevity and ease of application by water resource managers. Given the challenges regarding the application of shape metrics to

Table 1
Band wavelength ranges, lefts and widths for original and synthetic satellite imagers. FWHM is Full Width Half Maximum.

Imager	Original range (nm)	Center (nm)	FWHM (nm)	Synthetic range (nm)	Synthetic left (nm)	FWHM (nm)
WorldView-2/3				Resampled to 1.8 m		
b1	400–450	425	50	403–454	428.5	51
b2	450–510	480	60	454–505	479.5	51
b3	510–580	545	70	523–573	548	50
b4	585–625	605	40	582–633	607.5	51
b5	630–690	660	60	634–684	659	50
b6	705–745	725	40	710–749	729.5	39
b7	770–895	832.5	125	790–889	839.5	99
b8	860–1040	950	180	889–1043	966	154
Sentinel-2				Resampled to 20 m		
b1	433–453					
b2	458–523	490.5	65	457–515	486	58
b3	543–578	560.5	35	543–572	557.5	29
b4	650–680	665	30	643–686	664.5	43
b5	698–713	705.5	15	700–714	707	14
b6	733–748	740.5	15	728–743	735.5	15
b7	773–793	783	20	771–800	785.5	29
b8	785–900	842.5	115	785–900	842.5	115
b8b	855–875	865	20	856–871	863.5	15
b9	935–955	945	20	935–955	945	20
Landsat-8				Resampled to 30 m		
b1	430–450	440	20	429–443	436	14
b2	450–510	480	60	457–500	478.5	43
b3	530–590	560	60	529–586	557.5	57
b4	640–670	655	30	643–672	657.5	29
b5	850–880	865	30	856–885	870.5	29
MERIS/OLCI				Resampled to 300 m		
b1	402–412	407	10	400–414	407	14
b2	438–448	443	10	429–457	443	28
b3	485–495	490	10	486–500	493	14
b4	505–515	510	10	500–515	507.5	15
b5	555–565	560	10	558–572	565	14
b6	615–625	620	10	615–629	622	14
b7	660–670	665	10	657–672	664.5	15
b8	678–685	681.5	7	672–686	679	14
b9	704–714	709	10	700–714	707	14
b10	750–757	753.5	7	743–757	750	14
b11	757–762	759.5	5	750–764	757	14
b12	772–787	779.5	15	757–800	778.5	43
b13	855–875	865	20	842–885	863.5	43
b14	880–890	885	10	871–899	885	28
b15	895–905	900	10	885–913	899	28
MODIS				Resampled to 250 m		
b1	620–670	645	50	615–672	643.5	57
b2	841–876	858.5	35	842–871	856.5	29

Landsat-8 imagery, we also evaluated the 3BDA-like ("KIVU") (Brivio et al., 2001; Kneubuhler, Frank, Kellenberger, Pasche, & Schmid, 2007) and surface algal bloom index (SABI) (Alawadi, 2010). We eventually combined elements of many of the above algorithms (LaPotin, Kennedy, Pangburn, & Bolus, 2001) into two new algorithms specifically for Landsat-8. These new algorithms are FLH Blue and FLH Violet. We evaluated their performance as well so that water resource managers may compare them against existing algorithms for the estimation of Chl-*a* with satellite imagery (Table 3).

We followed the example of Kudela et al. (2015) and used a standard Type-1 regression test (Pinero, Perelman, Guerschman, & Paruleo, 2008) with twenty-nine points from water only pixels to compare the CASI and synthetic WorldView-2, Sentinel-2 and Landsat-8 imagery predictions on the X-axes to laboratory observations (measurements) of Chl-*a* (Sum_ReChl (Ug/L)) on the Y-axes to avoid mixed pixels that included the shoreline after rigorous quality control of coincident surface observations. Nine points were used to evaluate synthetic MODIS and MERIS imagery for the same reason. Measured Chl-*a* values were then compared to extracted image Chl-*a* index point values at each location and their statistical relationship evaluated with Pearson's r (Table 3).

We then used a standard Type 1 regression test for the Chl-*a* indices against measured Chl-*a* values to normalize all results to the same units to facilitate comparison of the performance of each algorithm following the method of Kudela et al. (2015) (Table 4). We used a critical p-value of 0.001 for all Pearson's r Type 1 regression tests in Tables 3 and 4 and Figs. 4, 6, 7, 8, 9 and 10.

Some researchers prefer Type 2 regressions (Peltzer, 2015) to test correlations of observed vs. measured values in natural systems. Therefore we also applied the Type 2 geometric mean method of Peltzer (2015) to Chl-*a* estimation at Harsha (East Fork) Lake with all results again normalized to calculated Chl-*a* values for top performing algorithms by Type 1 regression tests (Kudela et al., 2015) (Table 5).

2.8. Combined error budget

There are many potential sources of error in this study: the band math approach to simulating the upscaled imagery, the chlorophyll algorithms used, error in the surface observation data set, error from atmospheric correction and error from other image processing steps. As noted in our synthetic image discussion, previous studies estimate up to 8% relative error with our linear spectral binning technique and other techniques may double or halve this error (4–16%) (Schlapfer et al., 1999). Moreover, the radiometry of multispectral imagery simulated from hyperspectral imagery and real multispectral imagery may differ by up to twice (200%) pre-launch estimates (Jarecke et al., 2001). The differing spatial resolutions between the different imagers are more problematic and introduce radiometric errors on the order of 10–32% in similar imaging spectrometers (Schlapfer et al., 2002). Errors associated with the choice of atmospheric correction average 5–42% across most wavelengths for Visible through SWIR hyperspectral imagers (Kruse, 2004; Richter, 2008). Our total radiometric errors could be 282% or more accordingly and dwarfs errors associated with our choice of methods to synthesize satellite imagery from CASI hyperspectral data. Visual comparison of CASI reflectance and coincident surface spectra (Fig. 5) shows good agreement between 450 and 900 nm and poorer agreement above and below this wavelength range. Nonetheless, we see good agreement between the spatial patterns of image derived Chl-*a* estimates using several algorithms and laboratory measurements of Chl-*a* from coincident water samples as discussed below.

The purpose of this study is to synthetically create a "simultaneous" overpass of multiple (synthetic) imagers, apply feasible Chl-*a* algorithms to compare the performance of each algorithm/synthetic imager combination against the same set of dense, expensive and time consuming coincident surface (water) observations to suggest which algorithms are most likely to be the most portable between satellites. Given the numerous and poorly constrained sources of error associated with this study, calculated Chl-*a* values (Figs. 4c, 6c, 7c, 8c, 9c, and 10c) are included here only to facilitate a comparison of the relative performance of algorithm/synthetic imager combinations rather than to predict exact Chl-*a* concentrations with real-world imagers. Some of these synthetic imagers have not even been launched. Pre-launch and on-orbit radiometry often differ significantly as discussed above. Therefore real-world Chl-*a* concentration calibration for a full suite of imagers for smaller inland water bodies will require coincident surface (water) observations for each real world imagers although a comparison of their performance will be complicated by differences in their overpass times and dynamic environmental conditions.

3. Results and discussion

Single-band output from the Band Math function in ENVI for each Chl-*a* algorithm (Band Math Field in Table 2) was point sampled using the coincident surface observation locations to extract Chl-*a* index (image) values for comparison with measured Chl-values

Table 2
Band math and wavelengths in nm for each algorithm used for chlorophyll-*a* estimation at Harsha Lake. Float refers to floating point values.

Chl-*a* index algorithms by satellite/sensor	Spatial res. (m)	Band math/wavelengths (nm)
CASI CI	1	neg1*(((float(b23))-(float(b22))-((float(b25))-(float(b22))))))
CASI CI	1	neg1*(((float(686))-(float(672))-((float(714))-(float(672))))))
CASI MCI	1	(((float(b23))-(float(b22))-((float(b25))-(float(b22))))))
CASI MCI	1	(((float(686))-(float(672))-((float(714))-(float(672))))))
CASI FLH	1	(float(b25))-[float(b27) + (float(b23)-float(b27))]
CASI FLH	1	(float(714))-[float(743) + (float(686)-float(743))]
CASI NDCI	1	(float(b25)-float(b23))/(float(b25) + float(b23))
CASI NDCI	1	(float(714)-float(686))/(float(714) + float(686))
CASI 2BDA	1	(float(b25))/(float(b22))
CASI 2BDA	1	(float(714))/(float(672))
CASI 3BDA	1	((1/float(b22))-(1/float(b25)))*(float(b28))
CASI 3BDA	1	((1/float(672))-(1/float(714)))*(float(757))
WorldView-2 and -3 NDCI	1.8	(float(b6)-float(b5))/(float(b6) + float(b5))
WorldView-2 and -3 NDCI	1.8	(float(725)-float(660))/(float(725) + float(660))
WorldView-2 and -3 FLH violet	1.8	((float(b3))-[float(b5) + (float(b1)-float(b5))])
WorldView-2 and -3 FLH violet	1.8	((float(545))-[float(660) + (float(425)-float(660))])
WorldView-2 2BDA	1.8	(float(b6))/(float(b5))
WorldView-2 2BDA	1.8	(float(725))/(float(660))
WorldView-2 3BDA	1.8	((1/float(b5))-(1/float(b6)))*(float(b7))
WorldView-2 3BDA	1.8	((1/float(660))-(1/float(725)))*(float(833))
Sentinel-2 NDCI	20	(float(b5)-float(b4))/(float(b5) + float(b4))
Sentinel-2 NDCI	20	(float(705)-float(665))/(float(705) + float(665))
Sentinel-2 FLH violet	20	((float(b3))-[float(b4) + (float(b2)-float(b4))])
Sentinel-2 FLH violet	20	((float(560))-[float(665) + (float(490)-float(665))])
Sentinel-2 2BDA	20	(float(b5))/(float(b4))
Sentinel-2 2BDA	20	(float(705))/(float(665))
Sentinel-2 3BDA	20	((1/float(b4))-(1/float(b5)))*(float(b8b))
Sentinel-2 3BDA	20	((1/float(665))-(1/float(705)))*(float(865))
Landsat-8 NIR band is far from Chl-*a* peak		
Landsat-8 NDCI	30	(float(b5)-float(b4))/(float(b5) + float(b4))
Landsat-8 NDCI	30	(float(660)-float(605))/(float(660) + float(605))
Landsat-8 SABI	30	(float(b5)-float(b4))/(float(b2) + float(b3))
Landsat-8 SABI	30	(float(660)-float(605))/(float(480) + float(545))
Landsat-8 FLH blue	30	(float(b3)) + [float(b4) + (float(b2)-float(b4))]
Landsat-8 FLH blue	30	(float(545))-[float(605) + (float(480)-float(605))]
Landsat-8 FLH violet	30	(float(b3))-[float(b4) + (float(b1)-float(b4))]
Landsat-8 FLH violet	30	(float(545))-[float(605) + (float(425)-float(605))]
Landsat-8 2BDA	30	(float(b5))/(float(b4))
Landsat-8 2BDA	30	(float(660))/(float(605))
Landsat-8 KIVU (3BDA-like)	30	(float(b2)-float(b4))/(float(b3))
Landsat-8 KIVU (3BDA-like)	30	(float(480)-float(605))/(float(545))
MODIS NDCI	250	(float(b2)-float(b1))/(float(b2) + float(b1))
MODIS NDCI	250	(float(857)-float(646))/(float(857) + float(646))
MODIS 2BDA	250	(float(b2))/(float(b1))
MODIS 2BDA	250	(float(857))/(float(646))
MERIS CI	300	neg1*(((float(b8))-(float(b7))-((float(b9))-(float(b7))))))
MERIS CI	300	neg1*(((float(681))-(float(665))-((float(709))-(float(665))))))
MERIS MCI	300	(((float(b9))-(float(b8))-((float(b10))-(float(b8))))))
MERIS MCI	300	(((float(709))-(float(681))-((float(753))-(float(681))))))
MERIS FLH	300	(float(b9))-[float(b10) + (float(b8)-float(b10))]
MERIS FLH	300	(float(709))-[float(753) + (float(681)-float(753))]
MERIS NDCI	300	(float(b9)-float(b7))/(float(b9) + float(b7))
MERIS NDCI	300	(float(709)-float(665))/(float(709) + float(665))
MERIS 2BDA	300	(float(b9))/(float(b7))
MERIS 2BDA	300	(float(709))/(float(665))
MERIS 3BDA	300	((1/float(b7))-(1/float(b9)))*(float(b11))
MERIS 3BDA	300	((1/float(665))-(1/float(709)))*(float(761))

(Sum_ReChl_Ug_L) from water samples. All 44 sampling points were used to evaluate the performance of each algorithm applied to the CASI reflectance imagery. All of the synthetic imagery used for the following performance analysis with regard to the estimation of Chl-*a* are derived from VNIR CASI data atmospherically corrected to reflectance. Therefore, the following results are for atmospherically corrected imagery for all of the synthetic sensors considered below. We applied a standard Type 1 regression test (Pearson's r) for the Chl-*a* indices against measured Chl-*a* values to normalize all results to the same units to facilitate comparison of the performance of each algorithm (Fig. 4 and Table 4) following Pinero et al. (2008) and Kudela et al. (2015) as described in the Methods section above. We used 0.001 as our critical p value.

3.1. CASI imagery

We applied the CI, MCI, FLH, NDCI, 2BDA and 3BDA algorithms to the 1-meter, 48-band CASI VNIR hyperspectral reflectance image mosaic. All six algorithms applied to the imagery performed well due to the numerous narrow bands which are well suited to the CI, MCI, and FLH shape metric algorithms for the Chl-*a* peak between 700 and 714 nm (Gitelson, 1992; Zhao et al., 2010) and well placed for determining the slope of the (aquatic) "red" or "veg" (vegetation) edge (Shafique, Autrey, Fulk, & Cormier, 2001) (Table 1 and Figs. 4 and 5). The relatively long wavelength peak at 714 nm and high Chl-*a* concentration observed here is consistent with previous observations of a "red shift" at higher Chl-*a* concentrations (Vos et al., 1986; Gitelson, 1992). The CI, MCI,

Table 3
Performance of algorithms for chlorophyll-*a* estimation at Harsha Lake using Chl-*a* indices according to Pearson's r test (Type 1) linear regressions. Float refers to floating point values.

Chl-*a* index algorithms by satellite/sensor	No. of Water truth sites	Pearson's r	Pearson's r^2	p value	Slope	Intercept
	Sum_Rechl_Ug_L					
CASI CI	29	0.817	0.667	<0.001	0.152	36.648
CASI MCI	29	0.767	0.588	<0.001	0.188	18.324
CASI FLH	29	0.817	0.667	<0.001	0.152	36.648
CASI NDCI	29	0.829	0.687	<0.001	140.639	34.736
CASI 2BDA	29	0.847	0.717	<0.001	56.316	−19.899
CASI 3BDA	29	0.854	0.729	<0.001	98.773	36.311
WorldView-2 and -3 NDCI	29	0.851	0.724	<0.001	142.507	56.04
WorldView-2 and -3 FLH violet	29	0.728	0.530	<0.001	0.307	−52.569
WorldView-2 2BDA	29	0.843	0.711	<0.001	74.358	−19.085
WorldView-2 3BDA	29	0.861	0.741	<0.001	107.069	55.455
Sentinel-2 NDCI	29	0.891	0.794	<0.001	0.388	−18.844
Sentinel-2 FLH violet	29	0.598	0.358	<0.001	−0.033	53.064
Sentinel-2 2BDA	29	0.894	0.799	<0.001	86.148	−51.940
Sentinel-2 3BDA	29	0.832	0.692	<0.001	156.286	35.982
Landsat-8 NDCI	29	0.354	0.125	0.059	39.488	61.355
Landsat-8 SABI	29	0.351	0.123	0.062	67.034	64.569
Landsat-8 FLH blue	29	0.617	0.381	<0.001	0.360	−18.082
Landsat-8 FLH violet	29	0.740	0.548	<0.001	0.316	−46.053
Landsat-8 2BDA	29	0.395	0.156	0.034	27.122	29.244
Landsat-8 KIVU (3BDA-like)	29	−0.313	0.098	0.098	−217.99	5.078
Landsat-8 3BDA	29	0.398	0.158	0.033	27.122	29.244
MODIS NDCI	9	0.549	0.301	0.126	26.265	32.272
MODIS 2BDA	9	0.506	0.256	0.164	3.349	33.522
MERIS CI	9	0.917	0.841	<0.001	0.164	33.690
MERIS MCI	9	0.397	0.158	0.296	0.113	27.729
MERIS FLH	9	0.917	0.841	<0.001	0.164	33.690
MERIS NDCI	9	0.919	0.845	<0.001	155.920	37.724
MERIS 2BDA	9	0.918	0.843	<0.001	66.644	−28.538
MERIS 3BDA	9	0.912	0.832	<0.001	105.979	38.537

FLH, NDCI, 2BDA and 3BDA algorithms all performed well with this sensor in this experiment (Tables 2 and 3) with the 3BDA algorithm ranking slightly higher than the others. This algorithm does an excellent job of suppressing illumination between flight lines. The performance of each algorithm in Table 2 applied to the CASI imagery was evaluated using 29 coincident surface observations. These points were chosen to avoid pixels that mixed land, shadow and water at 1-meter spatial resolution.

Table 4
Performance of algorithms for chlorophyll-*a* estimation at Harsha (East Fork) Lake with all results normalized to calculated Chl-*a* values according to Pearson's r test (Type 1) linear regressions.

| Algorithms by satellite/sensor	Spatial res. (m)	Number of locations	p value	Sum_Rechl_Ug_L vs. Chl-*a* value	Sum_Rechl_Ug_L vs. Chl-*a* value	Sum_Rechl_Ug_L vs. Chl-*a* value
				Slope	Intercept	Pearson's r^2
CASI CI	1	29	<0.001	1.003	−0.098	0.667
CASI MCI	1	29	<0.001	1.001	−0.026	0.588
CASI FLH	1	29	<0.001	1.003	−0.098	0.667
CASI NDCI	1	29	<0.001	1.000	0.000	0.687
CASI 2BDA	1	29	<0.001	1.000	0.000	0.717
CASI 3BDA	1	29	<0.001	1.000	0.000	0.729
WorldView-2 and -3 NDCI	1.8	29	<0.001	1.000	0.000	0.724
WorldView-2 and -3FLH violet	1.8	29	<0.001	0.999	−0.078	0.530
WorldView-2 2BDA	1.8	29	<0.001	1.000	0.000	0.711
WorldView-2 3BDA	1.8	29	<0.001	1.000	0.000	0.741
Sentinel-2 NDCI	20	29	<0.001	1.000	0.001	0.794
Sentinel-2 FLH violet	20	29	<0.001	0.999	−0.021	0.358
Sentinel-2 2BDA	20	29	<0.001	1.000	0.000	0.799
Sentinel-2 3BDA	20	29	<0.001	1.000	−0.001	0.692
Landsat-8 NDCI	30	29	0.059	1.000	0.000	0.125
Landsat-8 SABI	30	29	0.062	1.000	0.000	0.123
Landsat-8 FLH blue	30	29	<0.001	1.000	0.001	0.381
Landsat-8 FLH violet	30	29	<0.001	1.000	−0.008	0.548
Landsat-8 2BDA	30	29	0.034	1.000	0.000	0.156
Landsat-8 KIVU (3BDA-like)	30	29	0.098	1.000	0.000	0.098
MODIS NDCI	250	9	0.126	1.000	0.000	0.301
MODIS 2BDA at 250 m res	250	9	0.164	1.000	−0.001	0.256
MERIS CI	300	9	<0.001	1.003	−0.097	0.841
MERIS MCI	300	9	0.290	1.003	−0.089	0.158
MERIS FLH	300	9	<0.001	1.000	−0.097	0.841
MERIS NDCI	300	9	<0.001	1.000	0.000	0.845
MERIS 2BDA	300	9	<0.001	1.000	0.000	0.843
MERIS 3BDA	300	9	<0.001	1.000	0.000	0.832
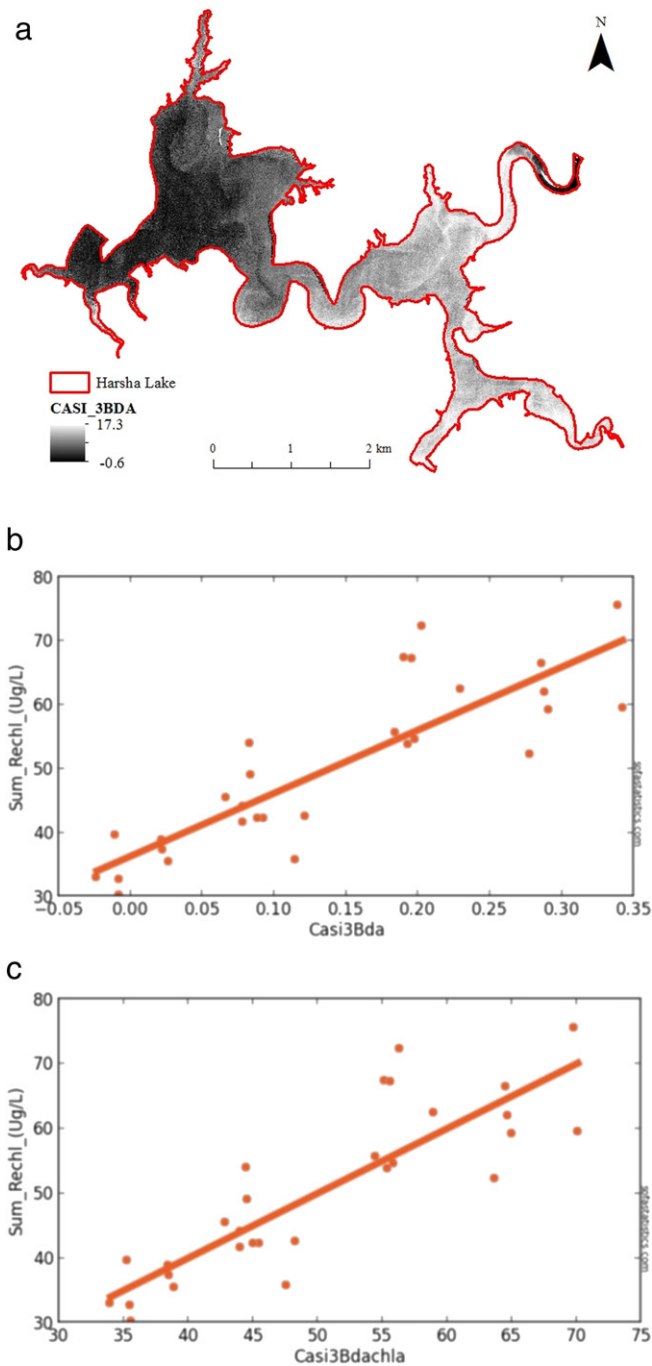
Fig. 4. Results of 3BDA algorithm (Mishra & Mishra, 2012) as raw index values as applied to original CASI imagery (shoreline in red) with brighter pixels in the reservoir indicating higher Chl-*a* concentrations (4a) and its evaluation via observed (Y axis = Sum_ReChl_Ug_L) vs. calculated raw 3BDA index value (Casi3Bda) with Pearson's r² (r² = 0.729, p < 0.001, N = 29 to avoid shorelines) (4b) and its evaluation via observed (Y axis = Sum_ReChl_Ug_L) vs. calculated Chl-*a* concentration (Casi3Bdachla) with Pearson's r² (r² = 0.729, p < 0.001, N = 29 to avoid shorelines) (4c). Details of the synthetic bands and band math are available in Tables 1 and 2 respectively.

3.2. WorldView-2 (synthetic)

We applied the NDCI, 2BDA, and 3BDA algorithms to synthetic 1.8-meter, WorldView-2 imagery to examine the degree of portability of some of the simpler algorithms between (synthetic) satellite imaging systems (Tables 1, 2, 3 and 4 and Fig. 6). We also applied a modified FLH

algorithm (focused on the green peak) that we developed for Landsat-8 (below) to WorldView-2 imagery for the same reason. All four algorithms performed well. The 3BDA algorithm had the best performance with regard to the estimation of Chl-*a* concentrations for this sensor in this experiment (Fig. 6). A new FLH Violet algorithm that we developed for Landat-8 (discussed below) also has good performance. The performance of each algorithm in Tables 2 and 3 applied to the synthetic WorldView-2 imagery was evaluated using 29 coincident surface observations. The simple ratio-based algorithms that include the reflectance in the near-infrared suppress illumination variation well and had the best performance with regard to Chl-*a* estimation.

3.3. Sentinel-2 (synthetic)

We also applied the NDCI, 2BDA, and 3BDA algorithms we used for WorldView-2 to the 20-meter, synthetic Sentinel-2 imagery. All three algorithms had acceptable performance with this sensor in this experiment and appear to have good portability between CASI, WorldView-2/-3 and Sentinel-2 imagery (Tables 3 and 4 and Fig. 7). The excellent performance of these three algorithms with synthetic Sentinel-2 imagery and their wide swaths and dual constellation suggests that Sentinel-2 satellites will play a key role in future monitoring systems for inland water quality. The 2BDA had very slightly better performance in this experiment and suppresses illumination variations between flight lines well. The performance of each algorithm in Tables 2 and 3 applied to the synthetic Sentinel-2 imagery was evaluated using 29 coincident surface observations coincident surface observations chosen to avoid pixels that mixed land and water at 20 and 30 m spatial resolutions. We also applied a modified FLH algorithm (focused on the green peak) that we developed for Landsat-8 (below) to our synthetic WorldView-2 imagery. Its performance with regard to Chl-*a* estimation was good but was surpassed by the other three ratio algorithms that suppress illumination variations and include the reflectance at the Chl-*a* near-infrared peak.

3.4. Landsat-8 (synthetic)

The widths and positions of Landsat-8 bands made the application of near-infrared Chl-*a* peak shape metrics infeasible and the application of some of the simple band ratio algorithms challenging (Tables 2 and 3, Fig. 8). We formulated two new FLH based algorithms focused on the visible green peak accordingly. Both measure the height of the green peak relative to the red and blue or violet minima. We refer to these algorithms as FLH Blue and FLH Violet respectively. The best performing algorithm was the green peak FLH Violet algorithm that incorporated the new ultra blue ("violet") coastal band for this sensor in this experiment.

The FLH algorithm does not suppress illumination variations between flight lines or scenes as well as the simpler ratio-based algorithms but still has relatively good performance. Algorithms for the estimation of Chl-*a* with synthetic Landsat-8 imagery were evaluated with the same 29 water truth sampling points as the Sentinel-2 data. Good performance of the FLH Violet Chl-*a* algorithm suggests that Landsat-8 may be a part of near-term operational monitoring systems for Chl-*a* in inland waters as a proxy for algal blooms. Future satellite imaging systems for HABs will require more numerous and more optimally placed narrow bands similar to those of WorldView-2/-3, Sentinel-2 and MERIS/OLCI.

3.5. MODIS (synthetic)

We applied the NDCI and 2BDA algorithms to synthetic MODIS bands 1 and 2 (Lindsey & Herring, 2001) with limited success (Tables 1, 2 and 3, Fig. 9). While MODIS could be a part of operational monitoring systems, its wide bands and coarse spatial resolution suggest that it will have limited value in operational monitoring systems

Table 5
Performance of algorithms for chlorophyll-*a* estimation at Harsha (East Fork) Lake with all results normalized to calculated Chl-*a* values with additional Type 2 Geometric Mean Tests (Peltzer, 2015) for top performing algorithms by Type 1 Regression tests (Kudela et al., 2015). The Type 2 regressions show a similar ordering of correlation with somewhat poorer results for Landsat-8 relative to Type 1 regressions on normalized calculated Chl-*a* values in Table 4.

Algorithms by Satellite/Sensor	Spatial res. (m)	N	Geometric mean slope	Geometric mean intercept	Geometric mean correlation coefficient squared	Standard deviation of slope	Standard deviation of Y-intercept
CASI 3BDA	1	29	1.171	−8.566	0.729	0.122	6.240
WorldView-2 and -3 3BDA	1.8	29	1.161	−8.067	0.741	0.118	6.032
Sentinel-2 2BDA	20	29	1.119	−5.956	0.799	0.099	5.097
Landsat-8 FLH violet	30	29	1.352	−17.638	0.546	0.188	9.567
MODIS NDCI	250	9	1.821	−38.205	0.301	0.654	30.584
MERIS NDCI	300	9	1.089	−4.118	0.845	0.165	7.834

for inland water quality, especially for smaller water bodies less than a few kilometers across. The performance of each algorithm in Tables 2 and 3 applied to the synthetic MODIS imagery was evaluated using nine coincident surface observations. These nine points were chosen to avoid pixels that mixed land and water at 250 and 300 m spatial resolutions. MODIS bands 1 and 2 were simulated with the CASI data at 250 m spatial resolution to facilitate comparison of algorithm performance. MODIS bands 1 and 2 are commonly available at the 250 m spatial resolution and are part of the better performing algorithm (NDCI). This suggests that MODIS NDCI may have some utility with regard to algal bloom monitoring in some larger inland water bodies. The large

pixel sizes associated with MODIS limit its use to relatively large water bodies and require severe masking to avoid mixed pixels.

3.6. MERIS (synthetic)

We applied the CI, MCI, FLH, NDCI, 2BDA and 3BDA algorithms to synthetic MERIS/OLCI data for Harsha Lake with limited success (Tables 2 and 3, Fig. 10) before severe masking. After severe masking all but one of the above algorithms performed well. NDCI was only slightly better than the CI, FLH, 2BDA and 3BDA algorithms in this experiment. We agree that MERIS/OLCI can be a part of operational water quality monitoring systems (Wynne et al., 2012). However, high-spatial resolution CASI data shows that there was significant spatial heterogeneity in the concentration of Chl-*a* on a scale much finer than either MERIS (300 m) or MODIS (250 m) pixels (Fig. 4). The greatest contribution of past MERIS studies for monitoring water quality in smaller inland water bodies less than a few kilometers across was the development of the Chl-*a* near infrared peak shape metrics (Wynne et al., 2012; Binding et al., 2013; Zhao et al., 2010), all of which performed well with real CASI and synthetic WorldView-2/-3 imagery but are not well suited to broad band multispectral imagery without significant modification and/or severe masking (Tables 2 and 3). This resulted in a limited number of pixels that emphasize the Chl-*a* contrast between the eastern (high concentrations) and western parts (low concentrations) of Harsha Lake during this study. Despite the many potential sources of error discussed above, our Chl-*a* concentration estimations are similar to (approximately twice) that of other studies focused on MERIS-like imagers (Mishra & Mishra, 2012). The NDCI Chl-*a* algorithm as applied to our synthetic MERIS data result in NDCI indices of 0 to 1.0 corresponding to Chl-*a* concentrations of approximately 37 to 55 $\mu g/m^3$. Mishra and Mishra (2012) found Chl-*a* concentrations of 16–25 $\mu g/m^3$ for the same NDCI index range. The difference may be due to environmental differences, different atmospheric correction techniques, our synthetic imager approximation technique or due to differences in the variety of laboratory and field techniques used to measure Chl-*a*. We have included very specific information regarding both our synthetic imaging technique as well as our laboratory and field Chl-*a* measurement techniques to aid future comparisons accordingly.

The Type 2 geometric mean regressions (Peltzer, 2015) show an ordering of correlation similar to those of Type 1 regressions (Pinero et al., 2008; Kudela et al., 2015) with somewhat poorer results for Landsat-8 (Table 5).

4. Conclusions

This study used atmospherically corrected high-spatial and high-spectral resolution VNIR CASI hyperspectral imagery to construct synthetic WorldView-2, Sentinel-2, Landsat-8, MODIS and Sentinel-3 (MERIS/OLCI) image data sets with dense coincident surface observations in the form of in situ water quality sonde and laboratory measurements to evaluate the performance of reflectance algorithms for estimating chlorophyll-*a* concentrations in a temperate reservoir in
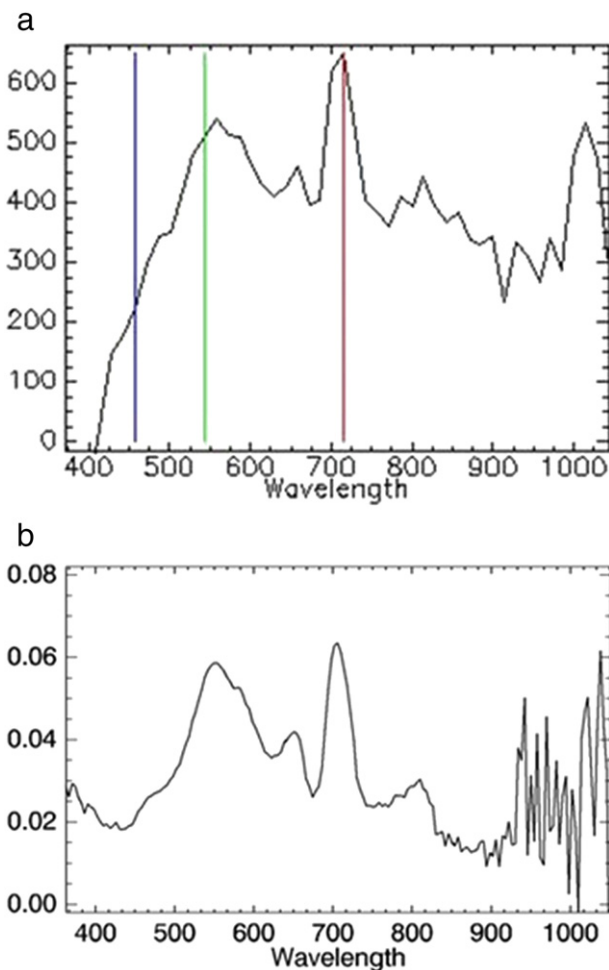
Fig. 5. Spectral profile from atmospherically corrected CASI data of water in NE Harsha Lake on the morning of 27 June 2014 (39° 01′ 16″ N; 84° 05′ 35″ W) showing a strong Chl-*a* reflectance peak in the near infrared at 714 nm (5a) and as measured at the water surface with a spectroradiometer in the field within 1 h of the overflight (5b). Y-axis is reflectance relative to calibration standards in both 5a and 5b scaled to 1000 and 1 respectively. Wavelength units are nanometers.
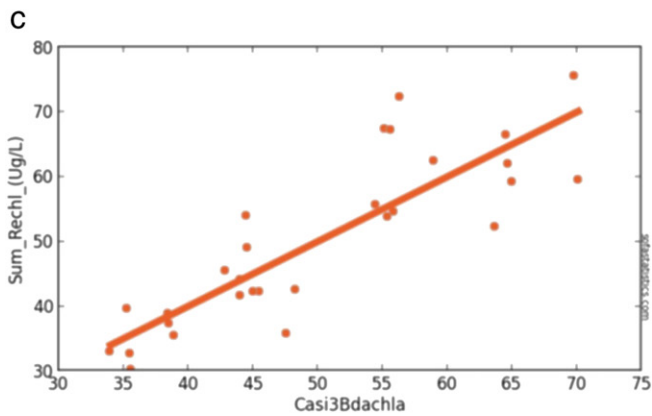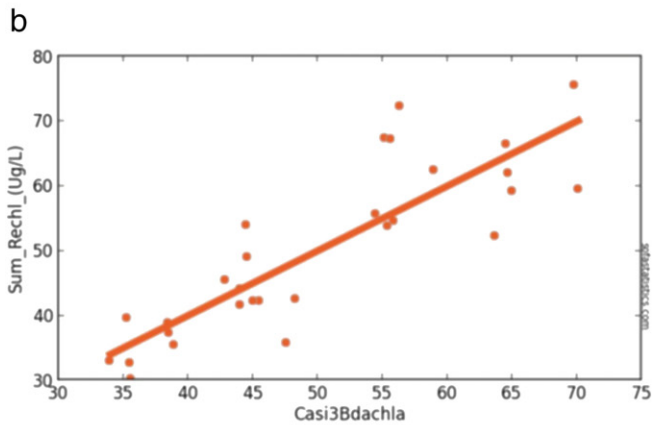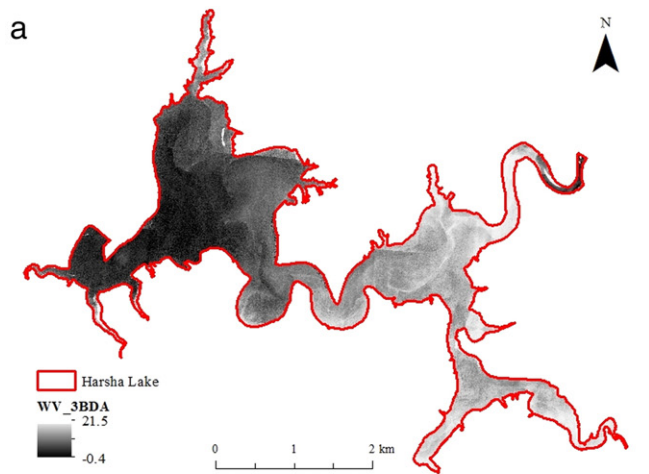
Fig. 6. Results of 3BDA algorithm (Mishra & Mishra, 2012) as raw index values as applied to synthetic WorldView imagery (shoreline in red) with brighter pixels in the reservoir indicating higher Chl-*a* concentrations (6a) and its evaluation via observed (Y axis = Sum_ReChl_Ug_L) vs. calculated raw 3BDA index value (Wv23_3Bda) with Pearson's r² (r² = 0.741, p < 0.001, N = 29 to avoid shorelines) (6b) and its evaluation via observed (Y axis = Sum_ReChl_Ug_L) vs. calculated Chl-*a* concentration (Wv23_3BDAchla) with Pearson's r² (r² = 0.741, p < 0.001, N = 29 to avoid shorelines) (6c). Details of the synthetic bands and band math are available in Tables 1 and 2 respectively.
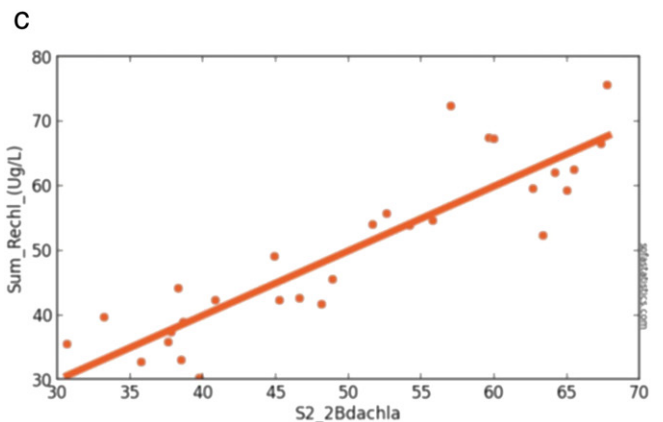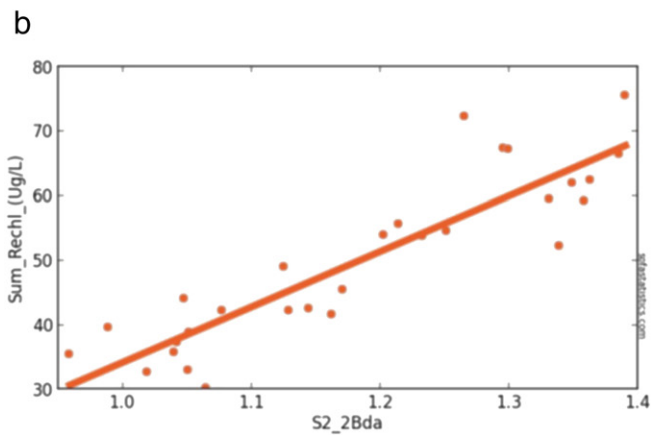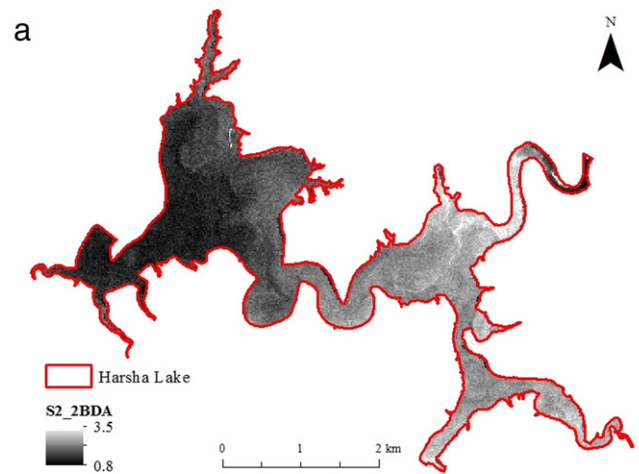
Fig. 7. Results of 2BDA algorithm (Mishra & Mishra, 2012) converted to Chl-*a* values as applied to synthetic Sentinel-2 imagery (shoreline in red) with brighter pixels in the reservoir indicating higher Chl-*a* concentrations (7a) and its evaluation via observed (Y axis = Sum_ReChl_Ug_L) vs. calculated raw 2BDA index value (S2_2Bda) with Pearson's r² (r² = 0.799, p < 0.001, N = 29 to avoid shorelines) (7b) and its evaluation via observed (Y axis = Sum_ReChl_Ug_L) vs. calculated Chl-*a* concentration (S2_2Bdachla) with Pearson's r² (r² = 0.799, p value <0.001, N = 29 to avoid shorelines) (7c). The CASI data allowed the synthesis of Sentinel-2 bands 2 through 9 only. Details of the synthetic bands and band math are available in Tables 1 and 2 respectively.

the manner of Augusto-Silva et al. (2014) as a proxy for algal blooms. The study focused on currently operational and near-future imaging satellite constellations that may be suitable contributors to an operational water quality monitoring system for inland reservoirs, lakes and rivers.

We found that several established algorithms for the estimation of Chl-*a* concentrations performed well for most of the synthetic satellite data sets considered here. The NDCI, 2BDA and 3BDA algorithms had the highest portability between the CASI, WorldView-2 and Sentinel-2 and MERIS-like imaging systems. Simple ratio-based algorithms
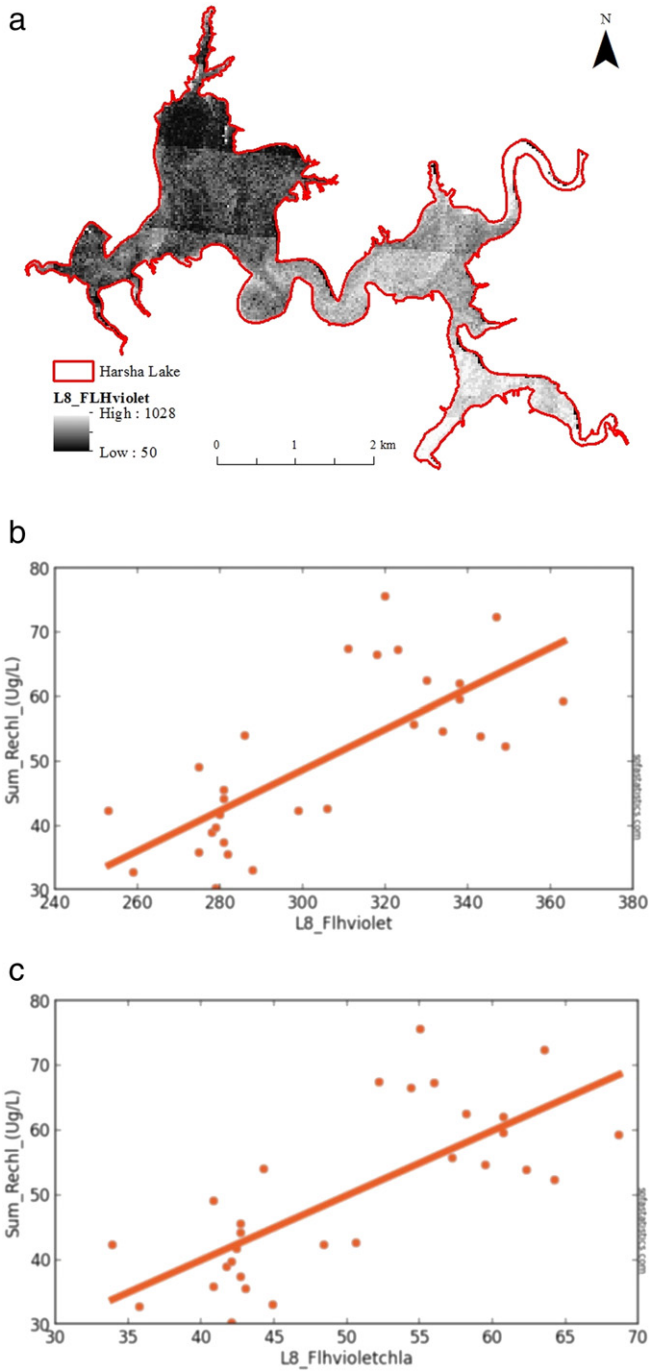
Fig. 8. Results of new FLH Violet algorithm (Mishra & Mishra, 2012) as raw index values as applied to synthetic Landsat 8 imagery (shoreline in red) with brighter pixels in the reservoir indicating higher Chl-*a* concentrations (8a) and its evaluation via observed (Y axis = Sum_ReChl_Ug_L) vs. calculated raw 2BDA index value (L8_Flhviolet) with Pearson's r² (r² = 0.548, p < 0.001, N = 29 to avoid shorelines) (8b) and its evaluation via observed (Y axis = Sum_ReChl_Ug_L) vs. calculated Chl-*a* concentration (L8_Flhvioletchla) with Pearson's r² (r² = 0.548, p < 0.001, N = 29 to avoid shorelines) (8c). Details of the synthetic bands and band math are available in Tables 1 and 2 respectively.

Fig. 9. Results of NDCI algorithm (Mishra & Mishra, 2012) converted to Chl-*a* values as applied to synthetic MODIS imagery (shoreline in red) with brighter pixels in the reservoir indicating higher Chl-*a* concentrations (9a) and its evaluation as raw index values as applied to synthetic MODIS imagery and its evaluation via observed (Y axis = Sum_ReChl_Ug_L) vs. calculated raw NDCI index value (Modis_Ndci) with Pearson's r² (r² = 0.301, p = 0.126, N = 9 due to large pixels) (9b) and its evaluation via observed (Y axis = Sum_ReChl_Ug_L) vs. calculated Chl-*a* concentration (Modis_Ndcichla) with Pearson's r² (r² = 0.301, p = 0.126, N = 9 due to large pixels) (9c). Details of the synthetic bands and band math are available in Tables 1 and 2 respectively.

suppress illumination variation between scenes and, when applied to imagers with relatively narrow bands that capture the Chl-*a* reflectance red minimum and near-infrared peak, estimate Chl-*a* concentrations well after imager and environment specific calibration. Landsat-8 requires an alternative algorithm such as our new FLH Violet algorithm. MERIS and MODIS do not capture the spatial heterogeneity in Chl-*a*
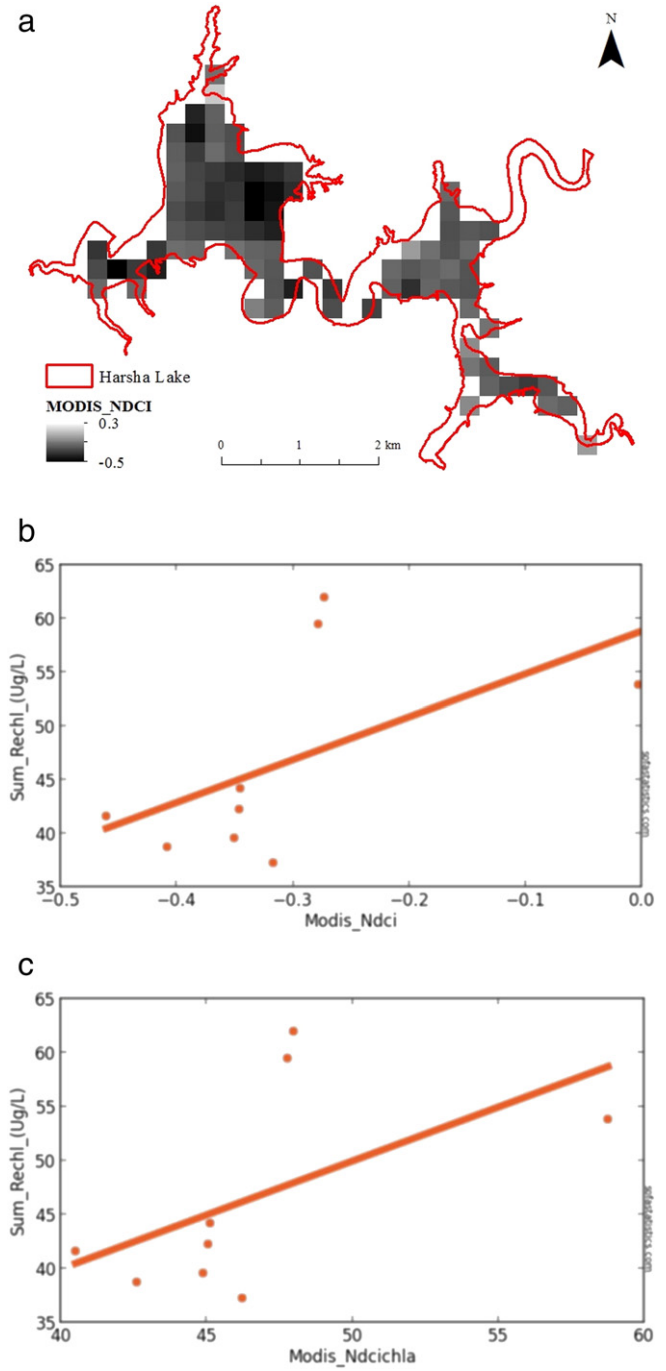
observed in this study due to their large pixels. MODIS has wide bands that do not target the "veg edge" or Chl-*a* reflectance peak well and has lower performance accordingly (Tables 2 and 3) although it may be useful with NDCI for larger water bodies.

For imagers with appropriate band widths and positions relative to the Chl-*a* reflectance signature and pixel sizes appropriate for the size
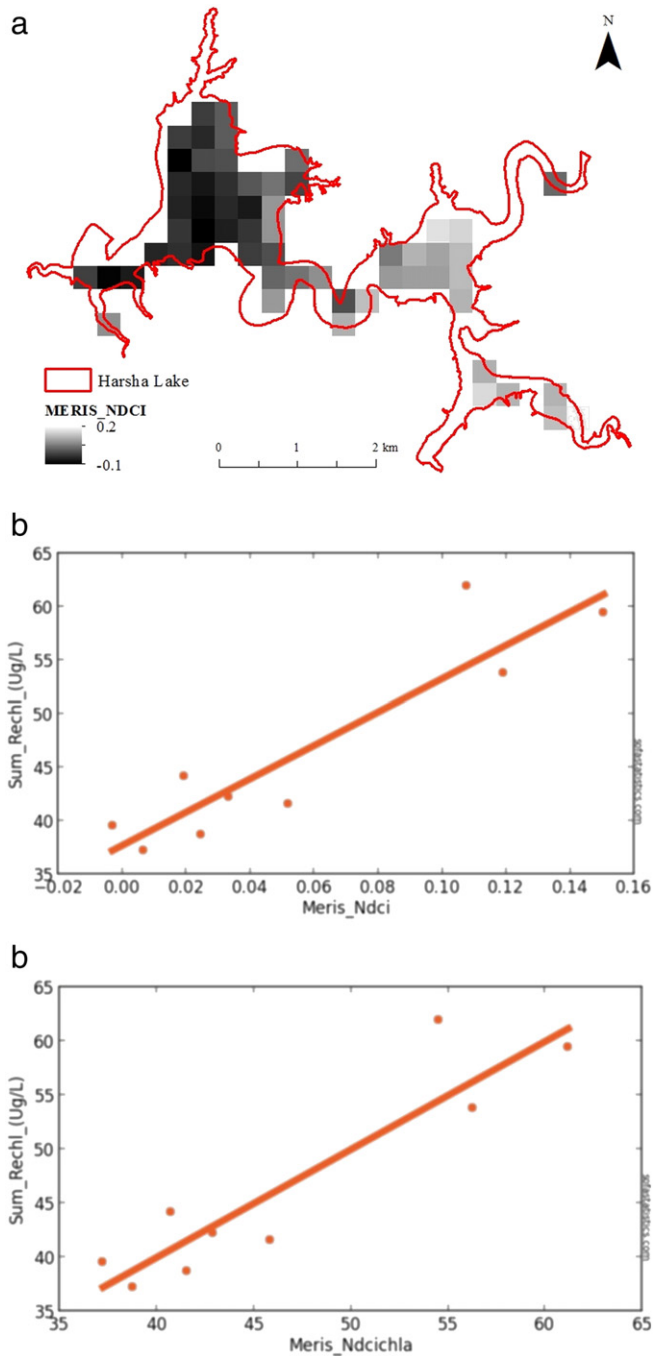
a

b

b

Fig. 10. Results of NDCI algorithm (Mishra & Mishra, 2012) as raw Chl-*a* index values as applied to synthetic MERIS imagery (shoreline in red) with brighter pixels in the reservoir indicating higher Chl-*a* concentrations (10a) and its evaluation via observed (Y axis = Sum_ReChl_Ug_L) vs. raw Chl-*a* index values (MerisNdci) concentration with Pearson's r^2 ($r^2 = 0.845$, $p < 0.001$, N = 9 due to large pixels) (10b) and its evaluation via observed (Y axis = Sum_ReChl_Ug_L) vs. calculated Chl-*a* (Merissynthcichla) concentration with Pearson's r^2 ($r^2 = 0.845$, $p < 0.001$, N = 9 due to large pixels) (10c). Details of the synthetic bands and band math are available in Tables 1 and 2 respectively.

of smaller inland water bodies, simple algorithms that ratio and therefore inherently normalize reflectance performed well and appear to be relatively portable between most satellite imaging systems for the estimation of Chl-*a* in smaller inland water bodies. Therefore, near-term steps toward operational water quality monitoring systems for inland water bodies smaller than a few kilometers across should focus on Sentinel-2A and B and Landsat-8 with augmentation from

WorldView-2 and -3 when required. MERIS/OLCI may also be useful for heavily masked time-series monitoring but will capture very little of the spatial heterogeneity of Chl-*a* concentrations in smaller inland water bodies.

Due to differing spatial and spectral resolutions and band locations not all algorithms could be applied to all synthetic imagers. We were able to apply two algorithms (NDCI and 2BDA) to all of the imagers and one algorithm (3BDA) to five imagers. All three performed well. NDCI is the most widely applicable algorithm and performs well with all of the synthetic imaging systems except Landsat-8 for which the new FLH Violet algorithm is recommended for the estimation of Chl-*a* in smaller inland water bodies. Interestingly, the performance of NDCI as measured by R^2 values, with the band approximations used in this study, improves from CASI (0.687) to synthetic WorldView-2/-3 (0.724) to synthetic Sentinel-2 (0.794) to synthetic MERIS (0.845) but performs poorly with synthetic Landsat-8 (0.125) and synthetic MODIS (0.301) imagery. The performance of 2BDA as measured by R^2 values is similar when applied to CASI (0.717) and synthetic WorldView-2/-3 (0.711) imagery and improves with synthetic Sentinel-2 (0.799) and synthetic MERIS (0.843) imagery but also performs poorly with synthetic Landsat-8 (0.156) and synthetic MODIS (0.256) imagery. In contrast, 3BDA performed very well with CASI (0.729) and synthetic WorldView-2/-3 (0.741) imagery, somewhat more poorly with synthetic Sentinel-2 (0.692) and better with synthetic MERIS (0.832) imagery. The 3BDA algorithm also performed poorly with synthetic Landsat-8 (0.158) imagery. Our results suggest that spatial averaging generally improves performance of the NDCI, 2BDA and 3BDA algorithms although the performance of large MERIS pixels may be exaggerated in this study by the strong contrast in Chl-*a* concentration between the eastern and western basins of Harsha Lake at the time of CASI image acquisition (Fig. 4a). Sentinel-2 appears to have an ideal combination of spatial and spectral resolutions for smaller inland water bodies and performs well with both the NDCI and 2BDA algorithms and continues to capture most of the spatial heterogeneity in Chl-*a* concentrations observed with higher CASI and synthetic WorldView data.

In general, the strong performance of the simple NDCI, 2BDA and 3BDA algorithms appears to be related to their ratio components that help to suppress variations in illumination and their exploitation of the "veg edge" associated with Chl-*a*. This later quality makes them amenable to many existing and near-future satellites designed to contrast the NIR and red contrast. The goal of this study was to evaluate the performance of a variety of algorithms with specific current and near-future imaging systems with specific combinations of spatial and spectral resolution in preparation for an operational algal bloom monitoring system. Future efforts will explore the relationships of spatial and spectral resolution on the performance of each algorithm individually. These efforts will help us to understand why some algorithms perform better than others.

These results address three of the research needs identified by Graham (2006) by; 1) quantitatively evaluating tools for monitoring algal blooms in general in temperate reservoirs; 2) contributing directly to the long-term Harsha Lake/EFWCoop study of environmental factors driving HAB formation and; 3) contributing to the development of methods for early algal bloom detection and ultimately predictive models for their formation in order to allow more time for resource managers to respond to potentially harmful algal blooms.

Future satellite imaging systems for inland water quality monitoring in water bodies smaller than a few kilometers will require spatial resolutions of 30 m or finer to capture the spatial heterogeneity observed during this experiment and spectral resolutions equal to or better than Sentinel-2 if they are to leverage the shape metric algorithms for the Chl-*a* peak near 710 nm. Interim systems such as PACE would add much needed temporal resolution and could be useful for inland water body algal bloom monitoring if their spatial resolutions were 90 m or finer and had narrow bands (<20 nm FWHM) at 620, 650 and

710 nm. Such future systems would have the advantage of using similar physics and algorithms across a number of satellite imaging constellations. Multiple constellations of imaging satellites totaling at least four satellites will be necessary for operational water quality monitoring systems due to frequent cloud cover in mid-latitude temperate climates. MERIS-like imagers with 300 m pixels may be able to detect changes in Chl-*a* concentrations over wide areas between overpasses for water bodies more than several pixels wide with heavy masking of shorelines and islands and deserve further study. Hybrid systems composed of a variety of imaging systems will benefit from atmospheric correction (Gao, Montes, Davis, & Goetz, 2009) and require calibration and validation experiments for each type of satellite imaging system once they are in orbit.

Author contributions

All authors played major roles in one of the most extensive coincident aircraft imaging, coincident surface observation and biogeochemical analysis campaigns for the evaluation of remote sensing algorithms for the estimation of water quality to date.

Acknowledgments

References

Alawadi, F. (2010). Detection of surface algal blooms using the newly developed algorithm surface algal bloom index (SABI). *Proceedings of SPIE*, 7825. http://dx.doi.org/10.1117/12.862096.

Allee, R. J., & Johnson, J. E. (1999). Use of satellite imagery to estimate surface chlorophyll *a* and Secchi disc depth of Full Shoals Reservoir, Arkansas, USA. *International Journal of Remote Sensing, 20*, 1057–1072.

American Public Health Association, American Water Works Association, & Water Environment Federation (2012). Spectrophotometric determination of chlorophyll: 10200H.2. In E. W. Rice, R. B. Baird, A. D. Eaton, & L. S. Clesceri (Eds.), *Standard methods for the examination of water and wastewater* (22nd ed.) (10–23:10–24).

Augusto-Silva, P. B., Ogashawara, I., Barbosa, C. C. F., de Carvalho, L. A. S., Jorge, D. S. F., Fornari, C. I., & Stech, J. L. (2014). Analysis of MERIS reflectance algorithms for estimating chlorophyll-*a* concentration in a Brazilian Reservoir. *Remote Sensing, 6*, 11689–117077.

Binding, C. E., Greenberg, T. A., & Bukata, R. P. (2013). The MERIS maximum chlorophyll index; its merits and limitations for inland water algal bloom monitoring. *Journal of Great Lakes Research, 39*, 100–107.

Blondeau-Patissier, D., Gower, J. F. R., Dekker, A. G., Phinn, S. R., & Brando, V. E. (2014). A review of ocean color remote sensing methods and statistical techniques for the detection, mapping and analysis of phytoplankton blooms in coastal and open oceans. *Progress in Oceanography, 123*, 123–144.

Borge, N. H., & Mortensen, J. V. (2002). Deriving green crop area index and canopy chlorophyll density of winter wheat from spectral reflectance data. *Remote Sensing of Environment, 81*, 45–57.

Brivio, P. A., Giardino, C., & Zilioli, E. (2001). Determination of chlorophyll concentration changes in Lake Garda using an image-based radiative transfer code for Landsat TM images. *International Journal of Remote Sensing, 22*, 487–502.

Cairns, S. H., Dickson, K. L., & Atkinson, S. F. (1997). An examination of measuring selected water quality trophic indicators with SPOT satellite HRV data. *Photogrammetric Engineering and Remote Sensing, 63*, 263–265.

Cannizzaro, J. P., & Carder, K. L. (2006). Estimating chlorophyll *a* concentrations from remote-sensing reflectance in optically shallow waters. *Remote Sensing of Environment, 101*, 13–24.

Chipman, J. W., Olmanson, L. G., & Gitelson, A. A. (2009). Remote sensing methods for lake management: A guide for resource managers and decision-makers. *Developed by the North American Lake Management Society in collaboration with Dartmouth College, University of Minnesota, and University of Nebraska for the United States Environmental Protection Agency*.

Choubey, V. K. (1994). Monitoring water quality in reservoirs with IRS-1A-LISS-I. *Water Resources Management, 8*, 121–136.

Dall'Olmo, G., & Gitelson, A. A. (2005). Effect of bio-optical parameter variability on the remote estimation of chlorophyll-*a* concentration in turbid productive waters: Experimental results. *Applied Optics, 44*, 412–422.

Dall'Olmo, G., Gitelson, A. A., & Rundquist, D. C. (2003). Towards a unified approach for remote estimation of chlorophyll-*a* in both terrestrial vegetation and turbid productive waters. *Geophysical Research Letters, 30*, 1038. http://dx.doi.org/10.1029/2003GL018065.

Dekker, A. G., & Peters, S. W. (1993). The use of the thematic mapper for the analysis of Eutrophic Lakes: A case study in The Netherlands. *International Journal of Remote Sensing, 14*, 799–822.

DigitalGlobe (2009). *WorldView-2 Data Sheet, 1–2.*

DigitalGlobe (2014). *WorldView-3 Data Sheet, 1–2.*

Ekstrand, S. (1992). Landsat TM based quantification of chlorophyll-*a* during algae blooms in coastal waters. *International Journal of Remote Sensing, 13*, 1913–1926.

European Space Agency (2012). *MERIS Frequently Asked Questions, 1–20.*

European Space Agency (2013). *Sentinel-2 Data Sheet, 1–2.*

Fraser, R. N. (1998). Hyperspectral remote sensing of turbidity and chlorophyll *a* among Nebraska Sand Hills lakes. *International Journal of Remote Sensing, 19*, 1579–1589.

Frohn, R. C., & Autrey, B. C. (2009). Water quality assessment in the Ohio River using new indices for turbidity and chlorophyll-*a* with Landsat-7 Imagery. *Draft Internal Report, U.S. Environmental Protection Agency*.

Gao, B., Montes, M. J., Davis, C. O., & Goetz, A. H. (2009). Atmospheric correction algorithms for hyperspectral remote sensing data of land and ocean. *Remote Sensing of Environment, 113*, S17–S24.

Giardino, C., Brando, V. E., Dekker, A. G., Strombeck, N., & Candiani, G. (2007). Assessment of water quality in Lake Garda (Italy) using Hyperion. *Remote Sensing of Environment, 109*, 183–195.

Gitelson, A. A., Nikanorov, A. M., Sabo, G., & Szilagyi, F. (1986). Etude de la qualite des eaux de surface par teledetection, monitoring to detect changes in water quality series. *Proceedings of the International Association of Hydrological Sciences, 157*, 111–121.

Gitelson, A. A. (1992). The peak near 700 nm on reflectance spectra of algae and water: Relationships of its magnitude and position with chlorophyll concentration. *International Journal of Remote Sensing, 13*, 3367–3373.

Gitelson, A. A., Garbuzov, G., Szilagyi, F., Mittenzwey, K. H., Karnieli, A., & Kaiser, A. (1993). Quantitative remote sensing methods for real-time monitoring of inland waters quality. *International Journal of Remote Sensing, 14*, 1269–1295.

Gitelson, A. A., Gritz, U., & Merzlyak, M. N. (2003). Relationships between leaf chlorophyll content and spectral reflectance and algorithms for non-destructive chlorophyll assessment in higher plant leaves. *Journal of Plant Physiology, 160*, 271–282.

Glasgow, H. B., Burkholder, J. M., Reed, R. E., Lewitus, A. J., & Kleinman, J. E. (2004). Real-time remote monitoring of water quality: A review of current applications, and advancements in sensor technology, telemetry, and computing technologies. *Journal of Experimental Marine Biology and Ecology, 300*, 409–448.

Gower, J., King, S., & Goncalves, P. (2008). Global monitoring of plankton blooms using MERIS MCI. *International Journal of Remote Sensing, 29*, 6209–6216.

Graham, J. L. (2006). Harmful algal blooms. *USGS Fact Sheet, 2006-3147.*

Han, L., Rundquist, D. C., Liu, L. L., Fraser, R. N., & Schalles, J. F. (1994). The spectral responses of algal chlorophyll in water with varying levels of suspended sediment. *International Journal of Remote Sensing, 15*, 3707–3718.

Hu, C., Barnes, B. B., Qi, L., & Crcoran, A. A. (2015). A harmful algal bloom of *Karenia brevis* in the Northeastern Gulf of Mexico as revealed by MODIS and VIIRS: A comparison. *Sensors, 15*, 2873–2887.

Hunter, P. D., Tyler, A. N., Willby, N. J., & Gilvear, D. J. (2008). The spatial dynamics of vertical migration by *Microcystis aeruginosa* in a eutrophic shallow lake: A case study using high spatial resolution time-series airborne remote sensing. *Limnology and Oceanography, 53*, 2391–2406.

Jarecke, P. J., Barry, P., Pearlman, J., & Markham, B. L. (2001). Aggregation of hyperion hyperspectral spectral bands into landsat-7 ETM+ spectral bands. In M. R. Descour, & S. S. Shen (Eds.), *Imaging Spectrometry VII. Proc. SPIE, 4480.* (pp. 259–263).

Kallio, K. (2000). Remote sensing as a tool for monitoring lake water quality. In P. Heinonen, G. Ziglio, & A. van der Beken (Eds.), *Hydrological and limnological aspects of lake monitoring* (pp. 237–245). Chichester, England: John Wiley & Sons, Ltd.

Klemas, V. (2012). Remote sensing of algal blooms: An overview with case studies. *Journal of Coastal Research, 28*(1A), 34–43.

Kneubuhler, M., Frank, T., Kellenberger, T. W., Pasche, N., & Schmid, M. (2007). Mapping chlorophyll-*a* in Lake Kivu with remote sensing methods. *Proceedings of the Envisat Symposium 2007, Montreux, Switzerland 23–27 April 2007 (ESA SP-636, July 2007)*.

Koponen, S., Pulliainen, J., Kallio, K., & Hallikainen, M. (2002). Lake water quality classification with airborne hyperspectral spectrometer and simulated MERIS data. *Remote Sensing of Environment, 79*, 51–59.

Kruse, F. A. (2004). *Comparison of ATREM, ACORN, and FLAASH atmospheric corrections using low-altitude AVIRIS data of Boulder. CO. Summaries of 13th JPL Airborne Geoscience Workshop* Pasadena CA: Jet Propulsion Lab.

Kudela, R. M., Palacios, S. L., Austerberry, D. C., Accorsi, E. K., Guild, L. S., & Torres-Perez, J. (2015). Application of hyperspectral remote sensing to cyanobacterial blooms in inland waters. *Remote Sensing of Environment, 1–10.* http://dx.doi.org/10.1016/j.rse.2015.01.025 (10 pp.).

LaPotin, P., Kennedy, R., Pangburn, T., & Bolus, R. (2001). Blended spectral classification techniques for mapping water surface transparency and chlorophyll concentration. *Photogrammetric Engineering and Remote Sensing, 67*, 1059–1065.

Lathrop, R. G., & Lillesand, T. M. (1986). Use of thematic mapper data to assess water quality in Green Bay and Central Lake Michigan. *Photogrammetric Engineering and Remote Sensing, 52*, 671–680.

Lindsey, R., & Herring, D. (2001). *Modis, 1–23.*

Linkov, I., Satterstrom, F. K., Loney, D., & Steevans, J. A. (2009). The impact of harmful algal blooms on USACE operations. *ANSRP technical notes collection. ERDC/TN ansrp-09-1.* Vicksburg, MS: U.S. Army Engineer Research and Development Center.

Matthews, A. M., Duncan, A. G., & Davison, R. G. (2001). An assessment of validation techniques for estimating chlorophyll-*a* concentration from airborne multispectral imagery. *International Journal of Remote Sensing, 22*, 429–447.

Mayo, M., Gitelson, A. A., Yacobi, Y. Z., & Ben-Avraham, Z. (1995). Chlorophyll distribution in Lake Kinneret determined from Landsat thematic mapper data. *International Journal of Remote Sensing, 16*, 175–182.

Mishra, S., & Mishra, D. R. (2012). Normalized difference chlorophyll index: A novel model for remote estimation of chlorophyll-*a* concentration in turbid productive waters. *Remote Sensing of Environment, 117*, 394–406.

Mittenzwey, K. -H., Ulrich, S., Gitelson, A.-. A., & Kondratiev, K. Y. (1992). Determination of chlorophyll *a* of inland waters on the basis of spectral reflectance. *Limnology and Oceanography, 37*, 147–149.

Morel, A., & Prieur, L. (1977). Analysis of variation in ocean color. *Limnology and Oceanography, 22*, 709–722.

Mustard, J. F., Staid, M. I., & Fripp, W. J. (2001). A semianalytical approach to the calibration of AVIRIS data to reflectance over water application in a temperate estuary. *Remote Sensing of Environment, 75*, 335–349.

Peltzer, E. T. (2015). Model 1 and model 2 regressions. http://www.mbari.org/staff/etp3/regress.htm (Last updated 18 May 2009, last accessed, 27 April 2015)

Quibell, G. (1992). Estimation of chlorophyll concentrations using upwelling radiance from different freshwater algal genera. *International Journal of Remote Sensing, 13*, 2611–2621.

Pinero, G., Perelman, S., Guerschman, J. P., & Paruleo, J. M. (2008). How to evaluate models: Observed vs. predicted or predicted vs. observed. *Ecological Modelling, 216*, 316–322.

Reif, M. (2011). Remote sensing for inland water quality monitoring: A U.S. Army Corps of Engineers Perspective. *Engineer Research and Development Center/Environmental Laboratory Technical Report (ERDC/EL TR)-11–13* (44 pp.).

Richter, R. (2008). *Atmospheric / topographic correction for satellite imagery. DLR IB 565-01/ 08, technical report* Germany: DLR Wessling available online at http://www.rese.ch/pdf/atcor23_manual.pdf

Rundquist, D. C., Han, L., Schalles, J. F., & Peake, J. S. (1996). Remote measurement of algal chlorophyll in surface waters: The case for the first derivative of reflectance near 690 nm. *Photogrammetric Engineering and Remote Sensing, 62*, 195–200.

Sauer, M. J., Roesler, C. S., Werdell, P. J., & Barnard, A. (2012). Under the hood of satellite empirical chlorophyll *a* algorithms: Revealing the dependencies of maximum band ratio algorithms on inherent optical properties. *Optics Express, 20*, 1–15.

Sawaya, K. E., Olmanson, L. G., Heinert, N. J., Brezonik, P. L., & Bauer, M. E. (2003). Extending satellite remote sensing to local scales: land and water resource monitoring using high-resolution imagery. *Remote Sensing of Environment, 88*(1–2), 144–156.

Schalles, J. F., Schiebe, F. R., Starks, P. J., & Troeger, W. W. (1997). Estimation of algal and suspended sediment loads (singly and combined) using hyperspectral sensors and integrated mesocosm experiments. *Proc. Fourth Int. Conf. Remote Sensing Mar. Coastal Environ., 17–19 March 1997, Orlando, Florida, 1.* (pp. 247–258). Ann Arbor: Environmental Research Institute of Michigan.

Schlapfer, D., Boerner, A., & Schaepman, M. (1999). The potential of spectral resampling techniques for the simulation of APEX imagery based on AVIRIS data. *NASA AVIRIS Workshop, 1999, no. 53* (pp. 1–7).

Schlapfer, D., Schaepman, M., & Strobl, P. (2002). Impact of spatial resampling methods on the radiometric accuracy of airborne imaging spectrometer data. *Conference: 5th Airborne Remote Sensing Conference and Exhibition, Miami/USA, 22–24 Mai.*

Shafique, N. A., Autrey, B. C., Fulk, F., & Cormier, S. M. (2001). Hyperspectral narrow wavebands selection for optimizing water quality monitoring on the Great Miami River, Ohio. *Journal of Spatial Hydrology, 1*, 1–22.

Shen, L., Xu, H., & Guo, X. (2012). Satellite remote sensing of harmful algal blooms (HABs) and a potential synthesized framework. *Sensors, 12*, 7778–7803.

Stumpf, R. P., & Tomlinson, M. (2005). *Remote sensing of harmful algal blooms. Remote sensing of coastal Aquatic environments.* Springer, 277–296.

Stumpf, R. P., Wynne, T. T., Baker, D. B., & Fahnenstiel, G. L. (2012). Interannual variability of cyanobacterial blooms in Lake Erie. *PloS One, 7*, 1–11.

Swayze, G. A., Clark, R. N., Goetz, A. F. H., Chrien, T. G., & Gorelick, N. S. (2003). Effects of spectrometer band pass, sampling, and signal-to-noise ratio on spectrometer identification using the Tetracorder algorithm. *Journal of Geophysical Research, 108*(E9), 5105. http://dx.doi.org/10.1029/2002JE001975.

Thiemann, S. T., & Kaufmann, H. (2002). Lake water quality monitoring using hyperspectral airborne data - A semiempirical multisensor and multitemporal approach for the Mecklenburg Lake District, Germany. *Remote Sensing of Environment, 81*, 228–237.

Thonfeld, F., Feilhauer, H., & Menz, G. (2012). Simulation of Sentinel-2 images from hyperspectral data. *Proceedings European Space Agency Conference* (http://www.congrexprojects.com/docs/12c04_docs2/poster2_43_thonfeld.pdf).

U.S. Environmental Protection Agency (USEPA) (2012). *Cyanobacteria and cyanotoxins: Information for drinking water systems.* U.S. Environmental Protection Agency, Office of Water (EPA-810F11001).

U.S. Geological Survey (2015). *Landsat-8 (L8) Data Users Handbook, 1–98.*

Verdin, J. P. (1985). Monitoring water quality conditions in a large western reservoir with Landsat imagery. *Photogrammetric Engineering and Remote Sensing, 51*, 343–353.

Veryla, D. L. (1995). *Satellite remote sensing of natural resources.* CRC Lewis (199 pp.).

Vicory, A. (2009). Intergovernmental cooperation and public-private partnerships for water quality management in the Ohio River Valley: The ORSANCO experience. *Michigan State University stormwater workshop, March 26, 2009.*

Vos, W. L., Donze, M., & Bueteveld, H. (1986). On the reflectance spectrum of algae in water: The nature of the peak at 700 nm and its shift with varying concentration. *Tech. Report, Communication on Sanitary Engineering and Water Management, Delft, The Netherlands* 86–22.

Wang, Y., Xia, H., Fu, J., & Sheng, G. (2004). Water quality change in reservoirs of Shenzen, China: Detection using Landsat/TM data. *The Science of the Total Environment, 328*, 195–206.

Wynne, T. T., Stumpf, R. P., Tomlinson, M. C., & Dyble, J. (2012). Characterizing a cyanobacterial bloom in western Lake Erie using satellite imagery and meteorological data. *Limnology and Oceanography, 55*, 2025–2036.

Zhao, D. Z., Xing, X. G., Liu, Y. G., Yang, J. H., & Wang, L. (2010). The relation of chlorophyll-*a* concentration with the reflectance peak near 700 nm in algae-dominated waters and sensitivity of fluorescence algorithms for detecting algal bloom. *International Journal of Remote Sensing, 31*, 39–48.